

SEARCH FOR $t\bar{t}Z' \rightarrow t\bar{t}t\bar{t}$ PRODUCTION IN THE MULTILEPTON FINAL STATE IN
 pp COLLISIONS AT $\sqrt{s} = 13$ AND 13.6 TEV WITH THE ATLAS DETECTOR

By

Hieu Le

A DISSERTATION

Submitted to
Michigan State University
in partial fulfillment of the requirements
for the degree of

Physics — Doctor of Philosophy

2025

ABSTRACT

Lorem ipsum dolor sit amet, consectetur adipiscing elit, sed do eiusmod tempor incididunt ut labore et dolore magna aliqua. Ut enim ad minim veniam, quis nostrud exercitation ullamco laboris nisi ut aliquip ex ea commodo consequat. Duis aute irure dolor in reprehenderit in voluptate velit esse cillum dolore eu fugiat nulla pariatur. Excepteur sint occaecat cupidatat non proident, sunt in culpa qui officia deserunt mollit anim id est laborum.

ACKNOWLEDGMENTS

Advisor: Reinhard Schwienhorst

Postdoc: Binbin Dong

Committee

MSU group

ATLAS analysis group

Friend: Daniel, Grayson, Bella, Eric, Jordan

Other friends: Jasper, Adam, Brittany

Parents

Spouse: Allen Sechrist

ATLAS in general & funding agencies

PREFACE

This is my preface. remarks remarks remarks

TABLE OF CONTENTS

List of Tables	vii
List of Figures	viii
KEY TO ABBREVIATIONS	ix
Roadmap	1
Chapter 1. Introduction	2
Chapter 2. Theoretical Overview	3
2.1 The Standard Model	3
2.1.1 Elementary particles	3
2.1.2 Mathematical formalism	4
2.1.3 Beyond the Standard Model	6
2.2 Four-top quark production	6
2.3 Collider physics	7
Chapter 3. LHC & ATLAS Experiment	8
3.1 The Large Hadron Collider	8
3.1.1 Overview	8
3.1.2 LHC operations	8
3.2 The ATLAS detector	9
3.2.1 Inner detector	10
3.2.2 Calorimeter systems	11
3.2.3 Muon spectrometer	13
3.2.4 Forward detectors	15
3.2.5 Magnetic systems	15
3.2.6 Trigger & data acquisition	15
Chapter 4. Data & Simulated Samples	17
4.1 Data samples	17
4.2 Monte Carlo samples	17
4.2.1 $t\bar{t}Z'$ signal samples	17
4.2.2 Background samples	18
Chapter 5. Particle Reconstruction & Identification	20
5.1 Primary reconstruction	20
5.1.1 Topological clusters	20
5.1.2 Tracks	21
5.1.3 Vertices	22
5.2 Jets	23

5.2.1	Flavor tagging	24
5.3	Leptons	27
5.3.1	Electrons	27
5.3.2	Muons	32
5.4	Missing transverse momentum	35
5.5	Overlap removal	36
Chapter 6.	Analysis Strategy	37
6.1	Event selection	37
6.1.1	Object definition	38
6.1.2	Trigger selection	40
6.1.3	Event categorization	40
6.2	Analysis regions	41
6.2.1	Signal regions	42
6.2.2	Control regions	42
6.2.3	Validation regions	44
6.3	Background estimation	45
6.3.1	Template fitting for fake/non-prompt estimation	47
6.3.2	Charge misidentification data-driven estimation	48
6.3.3	$t\bar{t}W$ background data-driven estimation	49
6.3.4	$t\bar{t}Z$ background validation	52
Chapter 7.	Systematic Uncertainties	53
7.1	Experimental uncertainties	53
7.1.1	Leptons	53
7.1.2	Jets	54
7.1.3	Missing transverse energy	56
7.2	Modeling uncertainties	56
7.2.1	Signal and irreducible background uncertainties	56
7.2.2	Reducible background uncertainties	56
Chapter 8.	Results	59
8.1	Profile likelihood fit	59
8.2	Fit results	59
8.3	Limits	59
8.4	Interpretation	59
Chapter 9.	Summary	60
References	61

List of Tables

Table 4.1: Summary of all Monte-Carlo samples used in this analysis.	19
Table 5.1: [16]	36
Table 6.1: Caption	39
Table 6.2: Caption	40
Table 6.3: Caption	42
Table 6.4: Caption	43
Table 6.5: Caption	46
Table 7.1: Summary of the experimental systematic uncertainties considered in this analysis.	57
Table 7.2: Summary of the experimental systematic uncertainties considered in this analysis.	58

List of Figures

Figure 5.1:	21
Figure 5.2:	[9] [24] [29]	26
Figure 5.3:	[6]	28
Figure 5.4:	[4]	29
Figure 5.5:	[4]	31
Figure 5.6:	[4]	32
Figure 5.7:	[14]	34

KEY TO ABBREVIATIONS

Physical & mathematical quantities

χ^2 chi-squared

ΔR angular distance

η pseudorapidity

E_T transverse energy

E_T^{miss} missing transverse momentum

\hat{H} Higgs oblique parameter

I weak isospin

L instantaneous luminosity

μ signal strength

p_T transverse momentum

Particles

b bottom quark

pp proton-proton

$t\bar{t}$ top/anti-top quark

$t\bar{t}t\bar{t}$ four-top-quark

tW single-top

Acronyms

1LOS one lepton, or two leptons of opposite charges

ATLAS A Toroidal LHC ApparatuS

BDT boosted decision tree

BSM Beyond the Standard Model

CERN European Organization for Nuclear Research

CMS Compact Muon Solenoid

CR control region

ECIDS Electron Charge ID Selector
GNN graph neural network
HLT High-Level Trigger
ID inner detector
JER jet energy resolution
JES jet energy scale
JVT Jet Vertex Tagger
L1 Level 1
LH likelihood
LLH log-likelihood
LO leading order
LAr liquid argon
LHC Large Hadron Collider
MET missing transverse energy
NF normalization factor
NLO next-to-leading order
NNLO next-to-next-to-leading order
NP nuisance parameter
OP operating point
PS parton shower
PDF parton distribution function
PCBT pseudo-continuous b -tagging
QED quantum electrodynamics
QCD quantum chromodynamics
QFT quantum field theory
QmisID charge mis-identification
SF scale factor

SM Standard Model

SR signal region

SSML two leptons of the same charge, or more than two leptons (multilepton)

TDAQ Trigger and Data Acquisition

Roadmap

1. Finish adding bullets for all sections 05/16

Remaining

 - introduction
 - higgs-top yukawa coupling, SMEFT & Higgs oblique parameter
 - collider physics
 - mc background samples
 - ttbar/ptrel/high pT calibration & results
2. Fill in details 05/23
 - Add missing figures
 - Add missing bib
3. Finalize analysis 05/30
4. String everything together
5. Miscellaneous/logistics (proofreading, review, ATLAS approval, etc.)
6. Submission to the graduate school 06/15
7. Defense 06/30

Chapter 1. Introduction

Chapter 2. Theoretical Overview

2.1 The Standard Model

- SM describes fundamental forces & elementary particles
- more descriptions (a bit of history + recent developments - higgs & neutrino masses) -
- limitations: gravity & general relativity, arbitrary free parameters

2.1.1 Elementary particles

- Bosons (Bose-Einstein statistics, integer spin) & fermions (Fermi-Dirac statistics, half-integer spin)
- Fermions - building blocks: quarks & leptons [protons/neutrons constituents?]
- Bosons - force carriers & interaction mediators (elementary bosons == gauge bosons
(chart of elementary particles here))

Fermions

- elementary particles
- half-integer spin

Quarks

- building blocks for hadrons & bosons
- up down — charm strange — bottom top [by order of discovery and mass]
- charge doublets: $+2/3$ and $-1/3$ charge
- color charge & color confinement in hadrons
- interacts with all 4 fundamental forces

Leptons

- electron — muon — tau + neutrino [by order of mass]
- charge -1, neutrinos charge neutral
- interacts with all forces except strong, neutrinos only weak and gravitational

Bosons

- force mediators
- integer spin

Scalar

- spin 0
- Higgs massive, charge neutral, provides rest mass for all elementary particles,

Vector

- spin 1
- W/Z (weak), photon (QED/electrodynamic), gluons (QCD/strong)
- photon/gluon massless, charge neutral, gluon carries color charge out of 8 combinations of quark colors (color octet)
- W/Z massive, charged/neutral

2.1.2 Mathematical formalism

- QFT: treats particles as excitations of corresponding quantum fields: fermion field ψ , electroweak boson fields $W_{1/2/3}$ & B , gluon field G_α , Higgs field ϕ
- Lagrangian: gauge QFT containing local gauge symmetries of $SU(3)_C \times SU(2)_L \times U(1)_Y$ and global Poincar symmetry: translational symmetry, rotational symmetry & special relativity frame invariance

- Noether's theorem: local symmetries \rightarrow strong/weak/EM, Poincar \rightarrow momentum, angular momentum & energy conservation
- unexpanded Lagrangian with description of each part: kinetic terms, coupling terms, mass/Higgs terms)

Quantum chromodynamics

- strong interaction, $SU(3)_C$ gauge group under Yang-Mills theory
- C = color charge conservation
- QCD Lagrangian, expansion & brief explanation

Electroweak

- unified weak & electromagnetic interactions, $SU(2)_L \times U(1)_Y$ gauge group
- L = left-handed chirality \rightarrow weak isospin (I) conservation
- Y = weak hyper charge conservation
- Q = charge conservation = $I_3 + 1/2Y$
- QED Lagrangian, expansion & brief explanation

Higgs mechanism

fermions & bosons still massless from previous section, resolved by introduction of the Higgs mechanism

(show Higgs field, potential & Lagrangian)

(show minimum of Higgs potential aka VEV)

—————[continue later]—————

2.1.3 Beyond the Standard Model

2.2 Four-top quark production

- Top: heaviest particle, strong coupling to many BSM particles in BSM models.
- 4top: xsec relevant to and enhanced by many BSM models
- Predicted by SM and observed [observation paper]
- Predicted xsec and observed xsec
- (insert Feynman diagrams)
- Decay products & final state topologies

Top-philic vector resonance

- (briefly introduce composite pseudo-nambu-Goldstone boson and motivation)
- hypothesis: top quark large mass results from high mixing between a "true" top quark and a colored, fermionic composite state
- composite vector resonance can be modeled as a top-philic Z' boson (without QCD color) or top-philic KK-gluon (with QCD color)
- color singlet vector boson (Z') model coupling strongly to top and weakly or not at all to others
- (show Lagrangian for interaction)
- two body decay Z' into $t\bar{t}$ with $m_{Z'}$ in TeV range \rightarrow top mass
- decay channels: $t\bar{t}Z'$ s & t channels, tWZ' , tjZ'
- (show decay width at LO)
- (Feynman diagrams here)

Higgs-top Yukawa coupling

(show Lagrangian of Higgs-top Yukawa coupling)

(show dependence of $t\bar{t}t\bar{t}$ xsec on Yukawa coupling at LO)

Effective field theory

SMEFT expanding on SM Lagrangian using higher order operators

(show EFT Lagrangian)

quick overview on SMEFT dimension-6 four-fermion operators for BSM interpretation

and Higgs oblique parameter

2.3 Collider physics

[pp collision, pdf, cross section, luminosity]

Luminosity

Proton-proton collisions

jets, parton shower, hadronization

Parton distribution function

Cross section

Chapter 3. LHC & ATLAS Experiment

3.1 The Large Hadron Collider

theoretical predictions are tested with experimental data obtained from particle accelerators
world's largest accelerator built by CERN situated on the border of Switzerland and France
has been operating since xxxx
lifetime divided into 3 runs, currently on Run 3 with planned upgrades on the horizon
responsible for a number of discoveries aka Higgs, etc.

3.1.1 Overview

[Basic info: location, size, main working mechanism, main detectors, main physics done]

- 27 km circumference, reusing LEP tunnels 175 m below ground level
- 7-13-13.6 TeV center of mass energies for pp collisions
- other than pp, also collides pPb, PbPb at 4 points with 4 main detectors: ATLAS, CMS (general purpose detectors), ALICE (heavy ion physics, ion collisions), LHCb (*b*-physics)

3.1.2 LHC operations

- focuses mainly on pp collisions for this thesis - beams split into bunches of 1.1×10^{11} protons with instantaneous luminosity of up to $2 \times 10^{34} \text{ cm}^{-2}\text{s}^{-1}$
- beam energies ramp up in other accelerators before injection, full ramp up to 6.5 GeV about 20 minutes

(insert full diagram of accelerator chain)

Linac 4: hydrogen atoms, accelerated up to 160 MeV

PSB: H atoms stripped of electrons before injection, accelerated to 2 GeV

PS: 26 GeV, SPS: 450 GeV

LHC: injection in opposite directions, 6.5 TeV per beam

Run 1: 2010-2012, Run 2: 2015-2018, Run 3: 2022-2025, HL-LHC: 2029-?

COM energies: 7 & 8 TeV, 13 TeV, 13.6 TeV, 13.6 & 14 TeV

inbetween periods: long shutdowns (LS1, LS2, LS3)

(add HL-LHC timeline graph)

(insert LHC SM processes cross sections chart)

Top quark production at the LHC

history (CDF/D0)

LHC as a top factory: show luminosity and cross section for top processes

couples to Higgs as heaviest elementary particle

Higgs produced mainly from ggH (90%) via top loop and from ttH

(Feynman diagram of related processes)

3.2 The ATLAS detector

multipurpose particle detector with a symmetric cylindrical geometry and a solid angle

coverage of almost 4π

44m long, 25m diameter

inner detector, solenoid/toroid magnet, EM & hadronic calorimeters, muon spectrometer

(insert figure)

right-handed cylindrical system, z-axis follows beamline, azimuthal and polar (0 in the beam direction) angles measured with respect to beam axis.

pseudorapidity $\eta = -\ln \tan(\theta/2)$, approaches $\pm \infty$ along and 0 orthogonal to the beamline

distance $\Delta R = \sqrt{\Delta\eta^2 + \Delta\phi^2}$

transverse energy $E_T = \sqrt{p_T^2 + m^2}$

transverse momentum p_T component of momentum orthogonal to the beam axis $p_T = \sqrt{p_x^2 + p_y^2}$

3.2.1 Inner detector

- measures tracks of charged particles with high momentum resolution ($\sigma_{p_T}/p_T = 0.05\% \pm 1\%$)
- covers particles with $p_T > 0.5 \text{ GeV}$, $|\eta| < 2.5$
 pixel detector -> semiconductor tracker -> transition radiation tracker, innermost to outermost
- pixel detector:
 - innermost, 250 μm silicon pixel layers
 - detects charged particles from electron-hole pair production in silicon
 - measures impact parameter resolution & vertex identification for reconstruction of short-lived particles
 - spatial resolution of 10 μm in the $R - \phi$ plane and 115 μm in the z-direction
 - 80.4m readout channels
- sct:

- surrounds pixel detector, silicon microstrip layers with 80 μm strip pitch
 - particle tracks cross 8 strip layers
 - measures particle momentum, impact parameters, vertex position
 - spatial resolution of 17 μm in the $R - \phi$ plane and 580 μm in the z-direction
 - 6.3m readout channels.
- trt:
 - outermost, layers of 4 mm diameter gaseous straw tubes with transition radiation material (70% $Xe + 27\% CO_2 + 3\% O_2$) & 30 μm gold-plated wire in the center
 - tubes 144 cm length in barrel region ($|\eta| < 1$), 37 cm in the endcap region ($1 < |\eta| < 2$), arranged in wheels instead of parallel to beamline)
 - gas mixture produces transition radiation when ionized for electron identification
 - resolution/accuracy of 130 μm for each straw tube in the $R - \phi$ plane
 - 351k readout channels

3.2.2 Calorimeter systems

surrounds the inner detector & solenoid magnet, covers $|\eta| < 4.9$ and full ϕ range. Alternates passive and active material layers. Incoming particles passing through calorimeter produce EM cascades or hadronic showers in passive layer. Energies deposited and convert to electric signals in active layers for readout.

EM calorimeter:

- innermost, lead-LAr detector (passive-

active)

- measures EM cascades (bremsstrahlung & pair production) produced by electrons/photons
- divided into barrel region ($|\eta| < 1.475$) & endcap regions ($1.375 < |\eta| < 3.2$) with transition region ($1.372 < |\eta| < 1.52$) containing extra cooling materials for inner detector
- end-cap divided into outer wheel ($1.372 < |\eta| < 2.5$) & inner wheel ($2.5 < |\eta| < 3.2$)
- higher granularity in ID ($|\eta| < 2.5$) range for electrons/photons & precision physics, coarser elsewhere for jet reconstruction & MET measurements

hadronic calorimeter:

- outermost
- measures hadronic showers from inelastic QCD collisions

- thick enough to prevent most particles showers from reaching muon spectrometer
- split into tile calorimeter in barrel region ($|\eta| < 1.0$) & extended barrel region ($0.8 < |\eta| < 1.7$), LAr hadronic end-cap calorimeter (HEC) in end-cap regions ($1.5 < |\eta| < 3.2$) & LAr forward calorimeters (FCal) in $3.1 < |\eta| < 4.9$ range.
 - tile calorimeters: steel-plastic scintillating tiles, readout via photomultiplier tubes
 - hec: behind tile calorimeters, 2 wheels per end-cap. copper plates-LAr. overlap with other calorimeter systems to cover for gaps between subsystems
 - fcal: 1 copper module & 2 tungsten modules-LAr. copper optimized for EM measurements, tungsten for hadronic.

3.2.3 Muon spectrometer

- ATLAS outermost layer. measures muon momenta & charge in range $|\eta| < 2.7$
- momentum measured by deflection in track from toroid magnets producing magnetic field orthogonal to muon trajectory
 - large barrel toroids in $|\eta| < 1.4$, strength 0.5 T
 - 2 smaller end-cap toroids in $1.6 < |\eta| < 2.7$, strength 1 T
 - transition region $1.4 < |\eta| < 1.6$, deflection provided by a combination of barrel and end-cap magnets
- chambers installed in 3 cylindrical layers, around the beam axis in barrel region & in planes perpendicular to beam axis in the transition and end-cap regions
- split into high-precision tracking chambers (monitored drift tubes & cathode strip chambers) & trigger chambers (resistive plate chambers & thin gap chambers)
- trigger chambers provide fast muon multiplicity & approximate energy range information with L1 trigger logic
 - mdt:

<ul style="list-style-type: none"> * range $\eta < 2.7$, innermost layer $\eta < 2.0$ * precision momentum measurement * layers of 30 mm drift tubes filled 	<ul style="list-style-type: none"> with 93% <i>Ar</i> & 7% <i>CO</i>₂, with a 50 μm gold-plated tungsten-rhenium wire at the center * muons pass through tube, ionizing gas and providing signals. Combining signals from tubes
--	--

- forms track
- * maximum drift time from wall to wire 700 ns
- * resolution: 35 μm per chamber, 80 μm per tube
- csc:
 - * forward region $2.0 < |\eta| < 2.7$, highest particle flux and density region
 - * multiwire proportional chambers with higher granularity, filled with 80% *Ar* & 20% *CO*₂
 - * shorter drift time than MDT, plus other features making CSC suitable for high particle densities and consequently able to handle background conditions
 - * resolution: 40 μm in bending η -plane, 5 mm in nonbending ϕ -plane due to coarser cathode segmentation, per CSC plane
- rpc:
 - * range $|\eta| < 1.05$
 - * provide fast meas
- tgc:
 - * range $1.05 < |\eta| < 2.7$

3.2.4 Forward detectors

- LUCID (LUminosity measurement using Cherenkov Integrating Detector): ± 17 m from interaction point, measures luminosity using pp scattering in the forward region
- ALFA (Absolute Luminosity for ATLAS): ± 240 m, measures pp scattering at small angles
- ZDC (Zero-Degree Calorimeter): ± 140 m, measures centrality in heavy-ion collisions

3.2.5 Magnetic systems

superconducting solenoid & toroid magnets cooled to 4.5 K with liquid helium

solenoid: 2.56 m diameter, 5.8 m length, 2 T strength axial magnetic field, encloses inner detector

toroid = barrel + endcap toroid x2

barrel toroid: 9.2/20.1 m inner/outer diameter, 25.3 m length, 0.5 T strength

endcap toroid: 1.65/10.7 m inner/outer diameter, 5 m length, 1 T strength

(show magnet system diagram)

3.2.6 Trigger & data acquisition

LHC produces large amount of data (40 MHz with 25 ns bunch crossing), necessitates a way to filter out trash from interesting events

handles online processing, selecting and recording interesting events for further offline processing and more in-depth analyses

- Level-1 (L1) trigger: online, fast hardware-based trigger, reduces to 100 kHz
 - L1 calorimeter triggers (L1Calo): selects high energy objects & MET
 - L1 muon triggers (L1Muon): selects using hit information from RPC & TGC
 - L1 topological trigger (L1Topo): select based on topological selection synthesized using information from L1Calo & L1Muon
 - Central Trigger Processor (CTP): uses L1Calo/Muon/Topo for final L1 trigger decision within $2.5 \mu\text{s}$ latency. Also identify regions of interest in η and ϕ to be processed directly by HLT
- L1 trigger information read out by Front-End (FE) detector electronics then sent to ReadOut Drivers (ROD) for preprocessing and subsequently to ReadOut System (ROS) to buffer
- High-Level Trigger (HLT): offline, software-based trigger, using dedicated algorithms and L1 output as input, reduces to 1 kHz
- Send to storage for analyses after HLT

overall trigger process reduces original collision data rate by a factor of about 10000 after HLT

(show TDAQ diagram)

Chapter 4. Data & Simulated Samples

4.1 Data samples

LHC Run 2 data collected at $\sqrt{s} = 13$ TeV between 2015-2018

luminosity 140 fb^{-1}

(include uncertainty for Run 2 only)

4.2 Monte Carlo samples

Monte Carlo simulated samples are used to estimate signal acceptance before unblinding, profile the physics background for the analysis and to study object optimizations.

Simulated samples for this analysis use are generated from ATLAS' generalized MC20a/d/e samples for Run 2, using full detector simulation (FS) based on Geant4.

4.2.1 $t\bar{t}Z'$ signal samples

Run 2 $t\bar{t}Z'$ sample

samples: 6 samples for each mass point from $[1, 1.25, 1.5, 2, 2.5, 3]$ TeV

generator: MADGRAPH5_AMC@NLO v.2.8.1p3.atlas9 at LO with NNPDF3.1LO pdf

event: PYTHIA8 [v.244p3.rangefix] using A14 tune & NNPDF2.3LO pdf

parameters:

- chirality θ : does not affect the strong production mode for $t\bar{t}Z'$, therefore picking default value $\pi/4$ to suppress loop-production of the Z' resonance
- top- Z' coupling $c_t = 1$

resonance width computed with MADGRAPH5_AMC@NLO to be 4% of model configuration
with these parameters

4.2.2 Background samples

Run 2 mc20 samples (2015-2018)

(show MC sample table)

(go in depth into each sample? briefly explain different generator, pdf and ps?)

Process	ME Generator	ME Order	ME PDF	PS	Tune	Sim.
Signals						
$t\bar{t}H/A$	MADGRAPH5_AMC@NLO	LO	NNPDF30 LO	PYTHIA8	A14	AF3
$t\bar{t}Z'/tjZ'/tWZ'$	MADGRAPH5_AMC@NLO	LO	NNPDF3.1LO	PYTHIA8	A14	FS
$t\bar{t}t\bar{t}$ and $t\bar{t}t$						
$t\bar{t}t\bar{t}$	MADGRAPH5_AMC@NLO	NLO	NNPDF3.0n1o	PYTHIA8	A14	AF3
	MADGRAPH5_AMC@NLO	NLO	MMHT2014LO	HERWIG7 H7-UE- MMHT		AF3
	SHERPA	NLO	NNPDF3.0 NNLO	HERWIG7 SHERPA		FS
	MADGRAPH5_AMC@NLO	LO	NNPDF2.31o	PYTHIA8	A14	AF3
$t\bar{t}V$						
$t\bar{t}H$	POWHEGBOX v2	NLO	NNPDF3.0n1o (mc20)	PYTHIA8	A14	FS
			PDF4LHC21 (mc23)			AF3
	POWHEGBOX v2	NLO	NNPDF3.0n1o	HERWIG7 H7.2- Default		FS
$t\bar{t}Z$	MADGRAPH5_AMC@NLO	NLO	NNPDF3.0 NNLO	PYTHIA8	A14	FS
$t\bar{t}W$	SHERPA	NLO	NNPDF3.0 NNLO	SHERPA	SHERPA	FS
	SHERPA	LO	NNPDF3.0 NNLO	SHERPA	SHERPA	FS
$t\bar{t}$ and Single-Top						
$t\bar{t}$	POWHEGBOX v2	NLO	NNPDF3.0n1o	PYTHIA8	A14	FS
tW	POWHEGBOX v2	NLO	NNPDF3.0n1o	PYTHIA8	A14	FS
$t(q)b$	POWHEGBOX v2	NLO	NNPDF3.0n1o (s)	PYTHIA8	A14	FS
			NNPDF3.0n1o 4f (t)			FS
tWZ	MADGRAPH5_AMC@NLO	NLO	NNPDF3.0n1o	PYTHIA8	A14	FS
tZ	MADGRAPH5_AMC@NLO	LO	NNPDF3.0n1o 4f	PYTHIA8	A14	FS
$t\bar{t}VV$						
$t\bar{t}WW$	MADGRAPH5_AMC@NLO	LO	NNPDF3.0n1o	PYTHIA8	A14	FS
	(mc20)					
	MADGRAPH (mc23)					FS
$t\bar{t}WZ$	MADGRAPH	LO	NNPDF3.0n1o	PYTHIA8	A14	AF3
$t\bar{t}HH$	MADGRAPH	LO	NNPDF3.0n1o	PYTHIA8	A14	AF3
$t\bar{t}WH$	MADGRAPH	LO	NNPDF3.0n1o	PYTHIA8	A14	AF3
$t\bar{t}ZZ$	MADGRAPH	LO	NNPDF3.0n1o	PYTHIA8	A14	AF3
$V(VV)+jets$ and VH						
$V+jets$	SHERPA	NLO	NNPDF3.0 NNLO	SHERPA	SHERPA	FS
$VV+jets$	SHERPA	NLO	NNPDF3.0 NNLO	SHERPA	SHERPA	FS
		LO ($gg \rightarrow VV$)				FS
$VVV+jets$	SHERPA	NLO	NNPDF3.0 NNLO	SHERPA	SHERPA	FS
VH	POWHEGBOX v2	NLO	NNPDF3.0 AZNLO	PYTHIA8	A14	FS

Table 4.1: Summary of all Monte-Carlo samples used in this analysis.

Chapter 5. Particle Reconstruction & Identification

Reconstruction software reconstructs basic objects from signals collected from the event: interaction vertices, tracks, topological clusters of energy deposits

These quantities then used to reconstruct physics objects i.e. particles (electron, muon), jets, MET

5.1 Primary reconstruction

5.1.1 Topological clusters

[21][27]

Topological cluster (topo-cluster): Clusters of topologically connected cell signals in the calorimeter at the EM scale. This scale does not consider loss of signal from hadrons. Singular hits without hits from neighboring cells are considered noise.

Done in an effort to extract signal while minimizing electronic effects and physical fluctuations. Used to reconstruct hadronic objects and particles decaying hadronically i.e. τ leptons

Signal hits with significance above a cell signal significance level $\varsigma_{\text{cell}}^{\text{EM}}$ are seeded in as part of a proto-cluster. Neighboring cells satisfying a cluster growth threshold are collected into the cluster.

Two clusters are merged if a cell is matched to both

If a cluster has two or more local signal maxima satisfying $E_{\text{cell}}^{\text{EM}} > 500 \text{ MeV}$, the cluster is split accordingly.

The process continues iteratively until all cells with significant signal efficiency have been matched to a cluster.

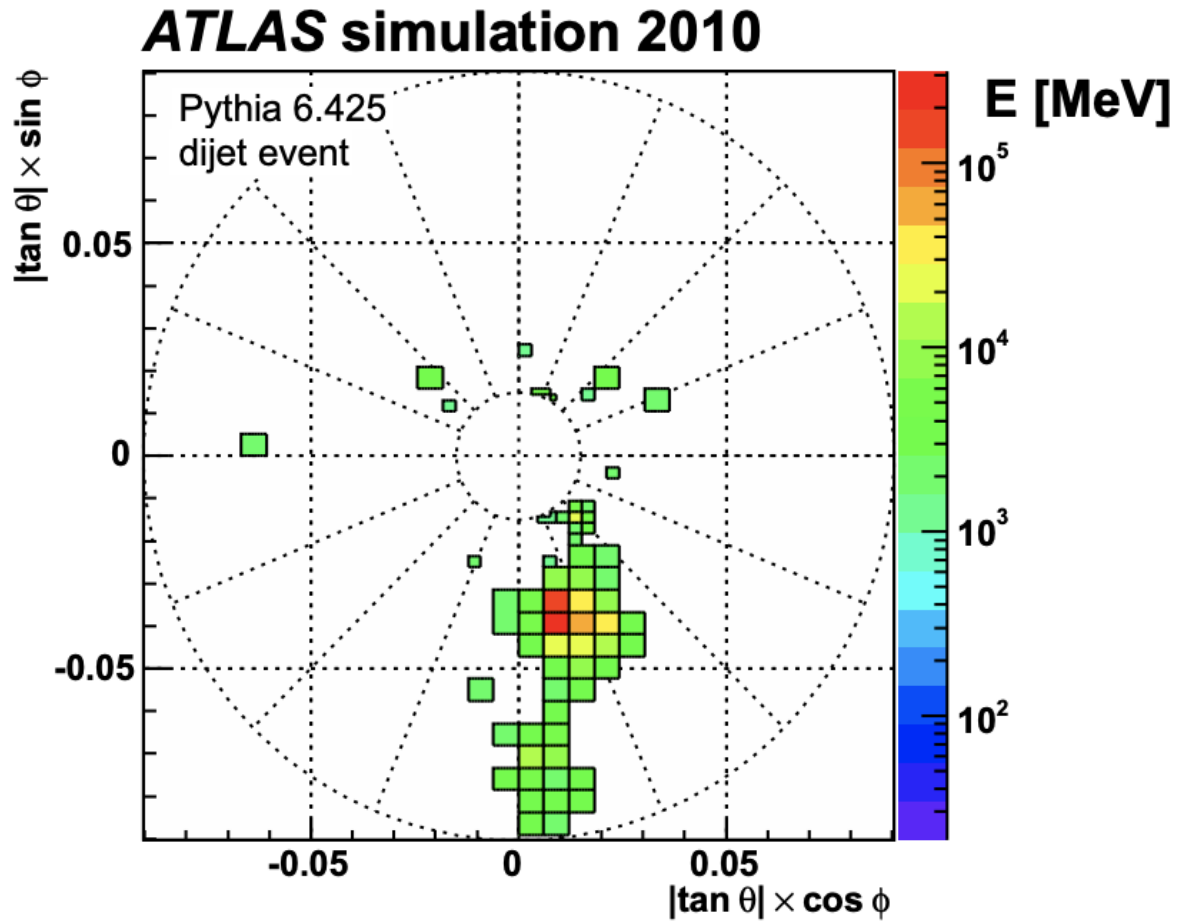


Figure 5.1

5.1.2 Tracks

[19]

Charged particles deposit energy in different layers of the inner detector and muon spectrometer

ID reco software: inside-out and outside-in algorithms

- Inside-out: [22]

Starts with seeded hits in the silicon detector in pixel & SCT

Loosely matched to an EM cluster to form a track candidate

Hits are added to form a track candidate using a pattern recognition algorithm based on a Kalman filter formalism [25]

Track candidates are then fitted with a χ^2 filter [23] and loosely matched to a fixed-sized EM cluster. Successfully matched track candidates are re-fitted with a Gaussian-sum filter (GSF) [10]

This is followed by a track scoring strategy to resolve fake tracks & hit ambiguity between different tracks [31]

Extend to TRT to form final tracks, filtered by threshold $p_T > 400$ MeV.

- Outside-in: [28]

Reverse, starts with segments in TRT extending inward to silicon hits in pixel & SCT

Targeting secondary tracks (decays/interactions of primary particles) or long-lived particles

5.1.3 Vertices

Vertices: interaction or decay point

Primary vertex: pp interaction point

Important for reconstruction of the hard scattering pp interaction, resulting trajectories and

kinematic information of the event

- Vertex finding:

Uses the z-position of a track as input

Vertices require to have at least 2 tracks

Iterative χ^2 algorithm evaluate track-vertex compatibility, using the track as new seed for another vertex if large discrepancy

- Vertex fitting:

Adaptive multi-vertex fitter (AVF) algorithm assigns weights that depend on the track-vertex compatibility to each track to measure the probability of the track being an outlier vs inlier.

Vertex is then estimated by iteratively minimizing an objective function of these weights

5.2 Jets

- Quarks, gluons & other non-color-neutral hadrons cannot be observed individually due to QCD color confinement

- A non-color-neutral hadron will almost immediately undergo hadronization producing a cone of color-neutral hadrons also known as a jet

- Jet signals can be used to reconstruct and consequently indirectly observe the original quarks/gluons the jets originated from

- Jet reconstruction:

- PFlow: energy deposited in the calorimeter systems by charged particles is removed and replaced by particle objects created with the remaining energy in the calorimeter and tracks matched to the topo-clusters. (include PFlow graphics)
- anti- k_t algorithms: sequential recombination jet algorithms
- pile-up jets: multiple interactions associated with one bunch crossing in addition to the hard scattering of interest and reconstructed as jets in the final states. Reconstructed pile-up jets can result from Pile-up jets are usually from soft interactions and can be distinguished with JVT algorithm using tracking information from the ID.
- JES/JER calibration: Jet reconstruction at EM scale does not accurately account for energy from QCD interactions and needs to be calibrated to jets reconstructed at particle level. This is done via a MC-based JES calibration sequence and additional JER calibration to match jet resolution in simulation to data using dijet events.

5.2.1 Flavor tagging

- Classification of hadronic jets is an important task for many LHC analyses especially ones studying final states (Higgs decay/4top)
- Flavor tagging is namely interested in identifying jets containing b -hadrons, c -hadrons, uds -hadrons (light-jets), and hadronic decays from τ .
- Of these, identifying b -jets is of particular interest due to their characteristically long lifetime (≈ 1.5 ps) from decay suppression by CKM factor, with a displaced secondary decay vertex and usually a tertiary vertex from c -hadron decays.

Efficiency calibration

- [12]

- Performance of b -taggers are studied on MC simulated samples. However, the b -tagging efficiency predicted by simulation $\varepsilon_b^{\text{sim}}$ is usually not the same as the efficiency measured in data $\varepsilon_b^{\text{data}}$.

- The correction for the rate of events after applying a b -tagging requirement is calibrated and applied jet by jet in the form of data-to-simulation scale factors $\text{SF} = \varepsilon_b^{\text{data}}/\varepsilon_b^{\text{sim}}$.

- Usage of b -tagger in this analysis is done via five operating points (OPs), corresponding to 60%, 70%, 77%, 85% and 90% b -jet tagging efficiency ε_b in simulated $t\bar{t}$ events in order from loosest to tightest discriminant cut points. - OPs are defined by selection on the tagger output to provide a pre-defined level of ε_b , and act as a variable trade-off between b -tagging efficiency and c -/light-jet rejection i.e. b -jet purity

- A jet is considered b -tagged if it passes the efficiency criteria for a given OP. A pseudo-continuous b -tagging (PCBT) score is defined to summarize the OP criteria a jet passes into a variable. The PCBT score can take integer values between 1 and 6, where a score of 6 means a jet passes all four OP thresholds (passing 65% OP), a score of 2 for jets that pass only the 90% OP, and a score of 1 for jets that don't pass any OP. Additionally, PCBT defines a value of -1 for any jet that does not satisfy b -tagging criteria.

- (insert TPR/FPR discriminant trade-off figure)

- $t\bar{t}$ bar calibration [2]

- ptrel and high pT calibration [30][13][3]
- impact parameter \rightarrow signed transverse impact parameter significance
- calibration results

GN2 b -tagging algorithm

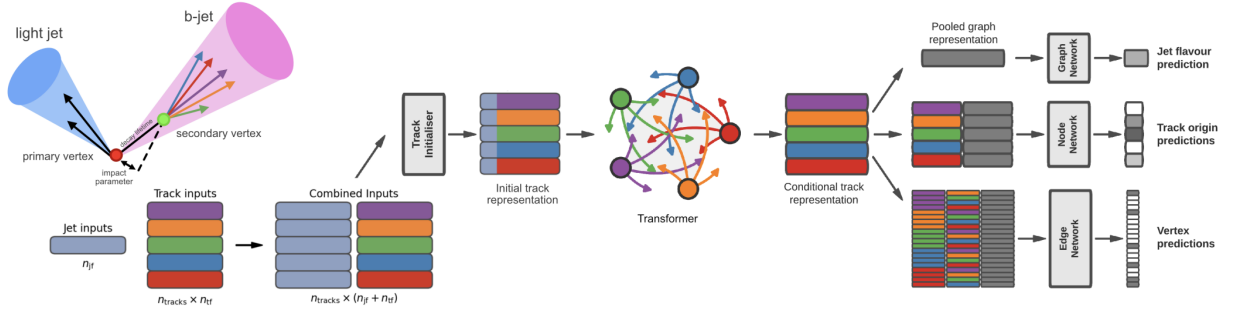


Figure 5.2: [9][24][29]

- GN2 transformer-based b -tagging algorithm, utilized for analysis of Run 2 and Run 3 data
- GN2 gives a factor of 1.5-4 improvement in experimental applications compared to the previous convolutional neural network-based standard b -tagging algorithm, DL1d, without dependence on the choice of MC event generator.
- Attention-based architecture, modified to incorporate domain knowledge and additional auxiliary physics objectives: grouping tracks originating from common vertices and prediction of the underlying process for each track
- MC simulated SM $t\bar{t}$ and BSM Z' events from pp collisions were used as training and evaluation samples. In order to minimize bias, both b - and light-jet samples are re-sampled to match c -jet distributions.
- GN2 concatenates 2 jet and 19 track reconstruction variables of up to 40 tracks to form

the input feature vector, normalized to zero mean and unit variance.

- The output consists of a jet classification layer of size 4 consisting of p_b , p_c , p_u and p_τ for the probability of each jet being a b -, c -, light- or τ -jet respectively; a track-pairing output layer of size 2, and a track origin classification layer of 7 output categories.

5.3 Leptons

- Lepton reconstruction is concerned mainly with electron and muon construction, since tau decays quickly and can either be reconstructed using jets or light leptons. From here on out lepton will be used mostly to refer to electrons and muons

- Leptons can be classified into two categories: prompt leptons resulting from heavy particle decays, or non-prompt leptons resulting from detector or reconstruction effects, or from b - or c - hadron decays

- Reconstruction of leptons is therefore important to study the underlying physics and suppressing background

5.3.1 Electrons

- [\[6\]](#)[\[4\]](#)

- Electrons lose energy interacting with the detector materials via bremsstrahlung. The bremsstrahlung photon can then produce an electron-positron pair which can itself leaves signals in the detector, creating a collimated object that can leave multiple tracks in the ID or EM showers in the calorimeter, all considered part of the same EM topo-cluster.

- Electron signal signature has three characteristic components: localized energy deposits in the calorimeter, multiple tracks in the ID and compatibility between the above tracks and

energy clusters in the $\eta \times \phi$ plane. Electron reconstruction in ATLAS follows these steps accordingly - Seed-cluster reconstruction and track reconstruction are performed sequentially

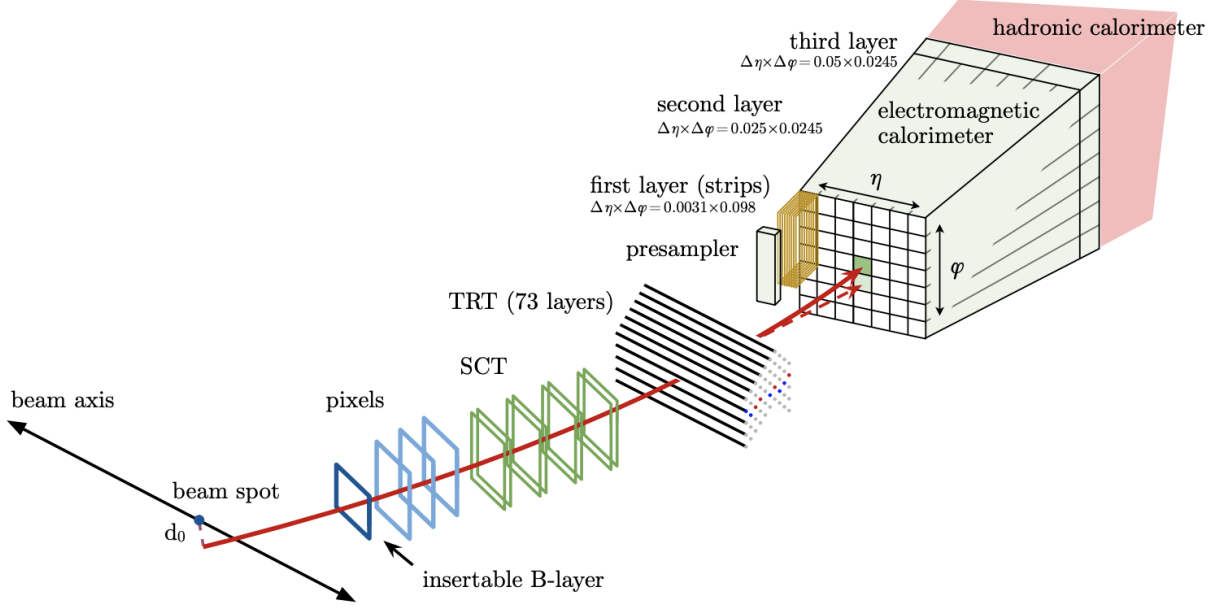


Figure 5.3: [6]

in accordance with the iterative clustering algorithm and track reconstruction method respectively, described in section 5.1

- The seed-cluster and track candidate associated with a conversion vertex are then matched to form an electron candidate.
- A reconstructed cluster is expanded from the seed-cluster in either ϕ or η in the barrel or endcap region respectively
- The cluster energy is then calibrated to compute the original electron energy.

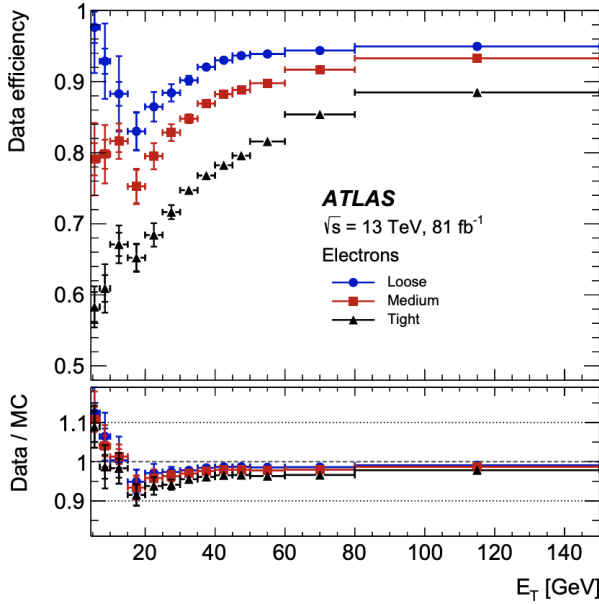
Electron identification

- Additional likelihood-based identification selections using ID and EM calorimeter information are implemented to further improve the purity of the reconstructed electrons and

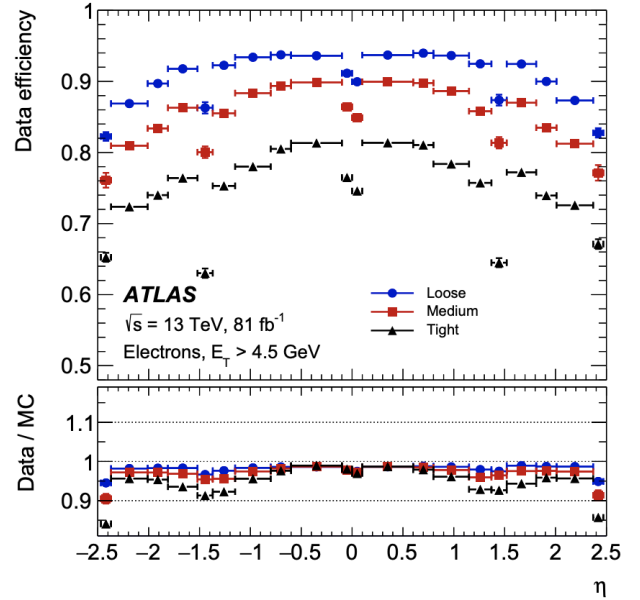
photons. These selections also help suppress background from hadronic jet deposits, photon conversions or electrons from heavy-flavor decays.

- Three operating points are defined for physics analyses: Loose, Medium and Tight, optimized for 9 bins in $|\eta|$ and 12 bins in E_T with each corresponding to a fixed efficiency requirement for each bin. The target efficiencies for Loose, Medium and Tight start at 93%, 88% and 80% respectively for typical EW processes and increases with E_T

Similar to b -tagging OPs, the electron OPs represent a trade-off in signal efficiency and background rejection. The electron efficiency are estimated using tag-and-probe method [6] on samples of $J/\Psi \rightarrow ee$ and $Z \rightarrow ee$.



(a) Figure A



(b) Figure B

Figure 5.4: [4]

Electron isolation

- A characteristic distinction between prompt electrons and electrons from background processes is the relative lack of activity in both the ID and calorimeter within an area of $\Delta\eta \times \Delta\phi$

surrounding the reconstruction candidate

- Electron isolation variables are needed to quantify the amount of activity around the electron candidate.
- Calorimeter-based isolation variables $E_T^{\text{cone}XX}$ is calculated by first summing the energy of topological clusters with barycenters falling within a cone of radius $\Delta R = \sqrt{(\Delta\eta)^2 + (\Delta\phi)^2} = XX/100$ around the direction of the electron candidate.
- The final isolation variable is then obtained by subtracting energy at the core of the cone belonging to the candidate electron from the sum, then applying corrections for energy leakage outside of the core and pile-up effects.
- Similar to calorimeter-based variables, track-based isolation variables $p_T^{\text{varcone}XX}$ are calculated by summing all track p_T within a cone of variable radius ΔR around the electron candidate, minus the candidate's contribution. The cone radius is variable as a function of p_T

$$\Delta R = \min \left(\frac{10}{p_T[\text{GeV}]}, \Delta R_{\text{max}} \right)$$

with ΔR_{max} being the maximum cone size, to account for the closer proximity of decay products to the electron in high-momentum heavy particle decays.

- Four isolation operating points are implemented to satisfy specific needs by physics analyses: Loose, Tight, HighPtCaloOnly and Gradient. The first three OPs are fixed in isolation variables, while the Gradient OP fixes the isolation efficiency to a p_T dependent function defined as $\varepsilon = 0.1143 \times p_T + 92.14\%$ with p_T in GeV, using $\Delta R = 0.2$ for calorimeter isolation and $\Delta R_{\text{max}} = 0.2$ for track isolation.

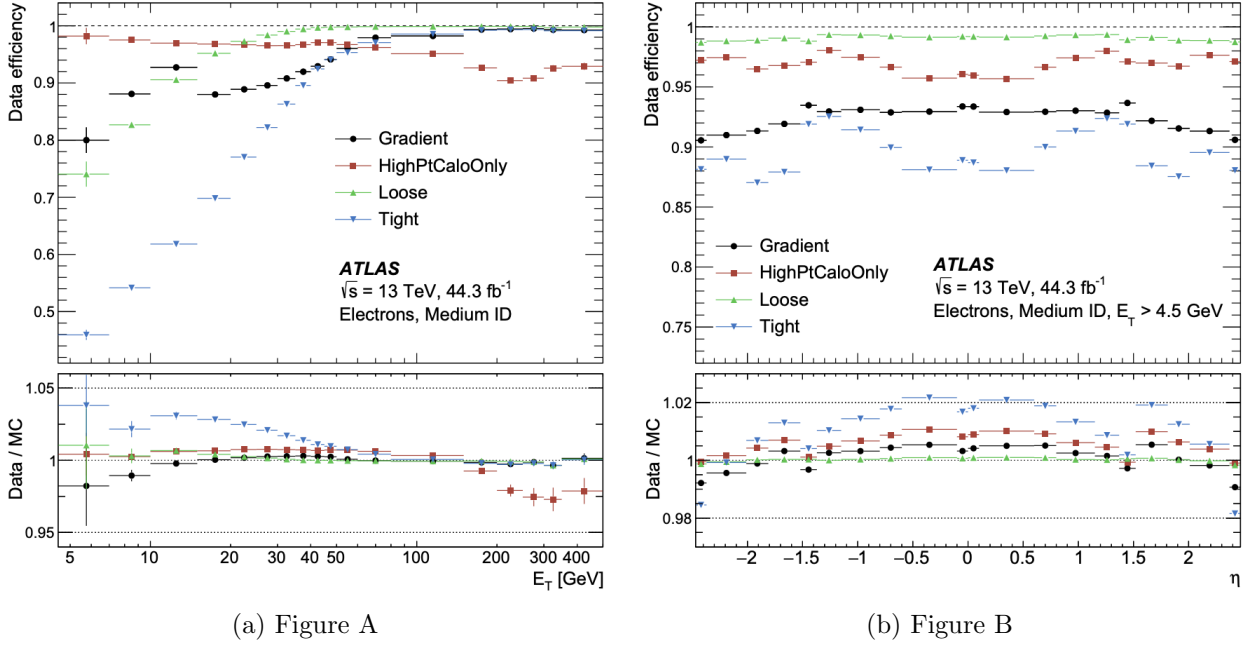


Figure 5.5: [4]

Electron charge misidentification

[6][5]

Electron charge is determined by the curvature of the associated track. Misidentification of charge can then occur via either an incorrect curvature measurement, or an incorrectly matched track.

The former is more likely for electrons with high p_T due to the small curvature in track trajectories at such scale, while the latter usually results from bremsstrahlung pair-production, creating additional secondary tracks in the vicinity.

Charge misidentification is a crucial irreducible background for analyses with charge selection criteria, and suppression of this background is assisted via a boosted decision tree discriminant known as the Electron Charge ID Selector (ECIDS) [6]. The addition of ECIDS removed 90% of electrons with incorrect charge while selecting 98% of electrons with correct

charge from electrons in $Z \rightarrow ee$ events satisfying Medium/Tight identification and Tight isolation criteria.

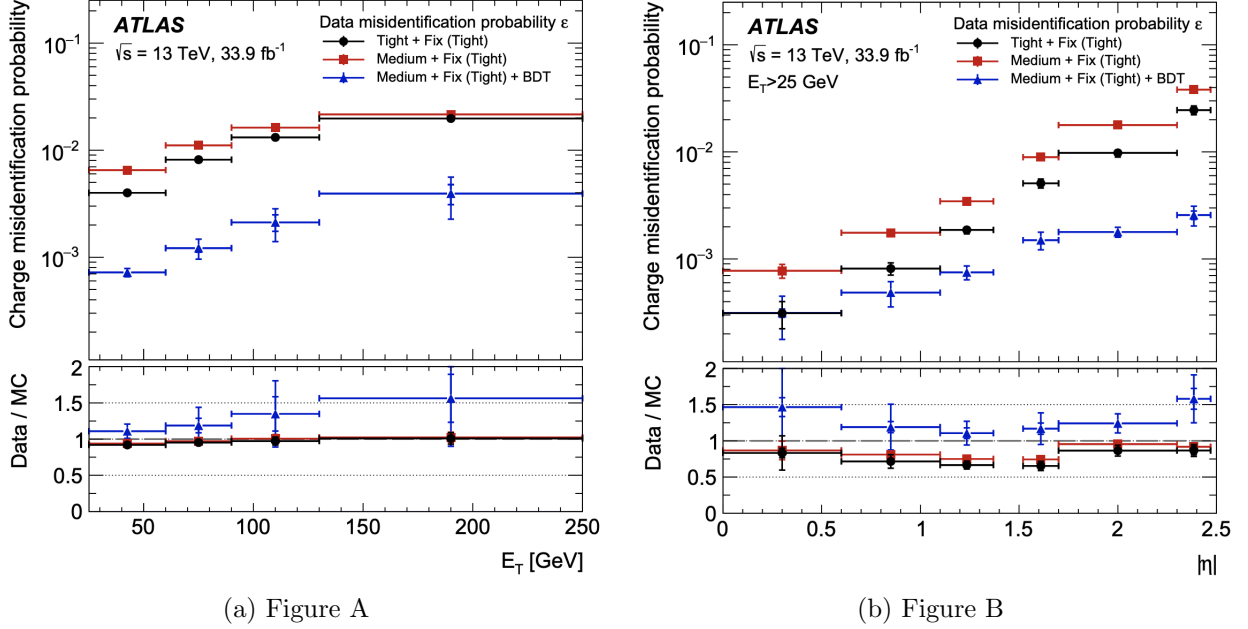


Figure 5.6: [4]

5.3.2 Muons

Signature: minimum-ionizing particle leaves tracks in the MS or characteristics energy deposits in the calorimeter

Muons can be reconstructed globally using information from the ID, MS and calorimeters.

Five reconstruction strategies, each corresponding to a muon type:

- Combined (CB): primary ATLAS muon reconstruction method. Muons first reconstructed using MS tracks then extrapolated to include ID tracks (outside-in strategy).

A global combined fit is then performed on both MS and ID tracks

- Inside-out combined (IO): Complementary to CB algorithm. Muon tracks are extrap-

olated from ID to MS, then fitted together with a combined track fit. Useful for muons without good MS information.

- MS extrapolated (ME): ME muons are defined as muons with a MS track that cannot be matched to an ID track using CB method. ME muons allow extension of muon reconstruction acceptance to regions not covered by the ID ($2.5 < |\eta| < 2.7$)
- Segment-tagged (ST): ST muons are ID tracks satisfying tight angular matching criteria to at least one reconstructed local segment in the MDT or CSC chambers when extrapolated to the MS. Used primarily when muons only crossed one layer of MS chambers.
- Calorimeter-tagged (CT): CT muons are ID tracks that when extrapolated through the calorimeter, can be matched to energy deposits consistent with those of a minimum-ionizing particle. Extends acceptance range to regions in the MS with sparse instrumentation ($|\eta| < 0.1$), with a higher p_T threshold of 5 GeV compared to 2 GeV threshold used by other muon reconstruction algorithms due to large background contamination at the low p_T range of $15 < p_T < 100$ GeV

Muon identification

[\[14\]](#)[\[15\]](#)

Reconstructed muons are further filtered by identification criteria to select for high-quality prompt muons for physics analyses. Requirements include number of hits in the MS/ID, track fit properties and compatibility between measurements of the two systems.

Three standard WPs (Loose, Medium, Tight) are defined to better match the needs of different physics analyses concerning prompt muon ID efficiency, p_T resolution and non-prompt

muon rejection. Of the three, Medium WP is the default ID WP for ATLAS, by virtue of being optimized in efficiency and purity for a wide range of analyses while minimizing non-prompt rejection and systematic uncertainties.

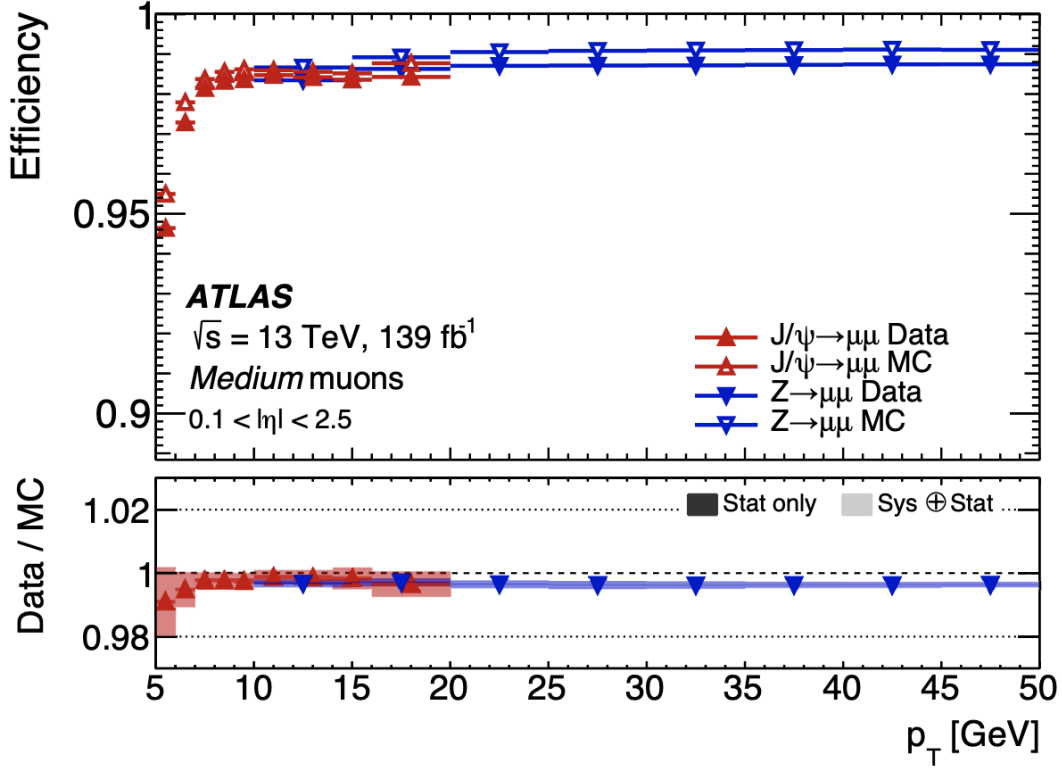


Figure 5.7: [14]

Muon isolation

Muons from heavy particle decays are often produced in an isolated manner compared to muons from semileptonic decays. Muon isolation is therefore an important tool for background rejection in physics analyses

Muon isolation strategies are similar to that of electron in Figure 5.3.1, with track-based and calorimeter-based isolation variables.

Seven isolation WPs are defined to satisfy analyses' needs.

5.4 Missing transverse momentum

[18]

Collisions at the LHC happen along the z-axis of the ATLAS coordination system between two particle beam of equal center-of-mass energy. By conservation of momentum, the sum of transverse momenta of outgoing particles should be zero. A discrepancy between measured momentum and zero would then suggest the presence of undetectable particles, which would consist of either SM neutrinos or some unknown BSM particles. This makes missing transverse momentum ($E_{\text{T}}^{\text{miss}}$) an important observable to reconstruct.

Reconstructing $E_{\text{T}}^{\text{miss}}$ utilizes information from fully reconstructed leptons, photons, jets and other matched track-vertex objects not associated with a prompt object (soft signals), defined with respect to the $x(y)$ -axis as

$$E_{x(y)}^{\text{miss}} = - \sum_{i \in \{\text{hard objects}\}} p_{x(y),i} - \sum_{j \in \{\text{soft signals}\}} p_{x(y),j}, \quad (5.1)$$

where $p_{x(y)}$ is the $x(y)$ -component of p_{T} for each particle. The following observables can then be defined:

$$\mathbf{E}_{\text{T}}^{\text{miss}} = (E_x^{\text{miss}}, E_y^{\text{miss}}), \quad (5.2)$$

$$E_{\text{T}}^{\text{miss}} = |\mathbf{E}_{\text{T}}^{\text{miss}}| = \sqrt{(E_x^{\text{miss}})^2 + (E_y^{\text{miss}})^2}, \quad (5.3)$$

$$\phi^{\text{miss}} = \tan^{-1}(E_y^{\text{miss}}/E_x^{\text{miss}}), \quad (5.4)$$

where E_T^{miss} represents the magnitude of the missing transverse energy vector $\mathbf{E}_T^{\text{miss}}$, and ϕ^{miss} its direction in the transverse plane. Since physics analyses have differing requirements for object selection, the vectorial sum $\mathbf{E}_T^{\text{miss}}$ can be broken down into

$$\mathbf{E}_T^{\text{miss}} = - \underbrace{\sum_{\text{selected electrons}} \mathbf{p}_T^e - \sum_{\text{selected muons}} \mathbf{p}_T^\mu - \sum_{\text{accepted photons}} \mathbf{p}_T^\gamma - \sum_{\text{accepted } \tau\text{-leptons}} \mathbf{p}_T^\tau - \sum_{\text{accepted jets}} \mathbf{p}_T^{\text{jet}}}_{\text{hard term}} - \underbrace{\sum_{\text{unused tracks}} \mathbf{p}_T^{\text{track}}}_{\text{soft term}}. \quad (5.5)$$

Two WPs are defined for E_T^{miss} , Loose and Tight [7], with selections on jet p_T and JVT criteria. The Tight WP reduces pileup dependence of E_T^{miss} by removing the phase space region with more pileup jets than hard-scatter jets, at the expense of resolution at low pileup and scale of the reconstructed E_T^{miss} .

5.5 Overlap removal

Since the reconstruction processes for different objects are performed independently, it is possible for the same detector signals to be used to reconstruct multiple objects. An overlap removal strategy to resolve ambiguities; the overlap removal process for this analysis applies selections listed in Table 5.1 sequentially, from top to bottom.

Remove	Keep	Matching criteria
Electron	Electron	Shared ID track, $p_{T,1}^e < p_{T,2}^e$
Muon	Electron	Shared ID track, CT muon
Electron	Muon	Shared ID track
Jet	Electron	$\Delta R < 0.2$
Electron	Jet	$\Delta R < 0.4$
Jet	Muon	$(\Delta R < 0.2 \text{ or ghost-associated}) \ \& \ N_{\text{track}} < 3$
Muon	Jet	$\Delta R < \min(0.4, 0.04 + 10\text{GeV}/p_T^\mu)$

Table 5.1: [16]

Chapter 6. Analysis Strategy

6.1 Event selection

Events for the analysis first are preselected following a list of criteria to optimize for event quality and background rejection.

The criteria are applied sequentially, from top to bottom

1. **Good Run List (GRL):** data events must be part of a predefined list of suitable runs and luminosity blocks.
2. **Calorimeter cleaning:** events containing signal hits indicating an error in the calorimeter are removed.
3. **Primary vertex:** events must have at least one reconstructed vertex matched to 2 or more associated tracks with $p_T > 500$ MeV.
4. **Trigger:** events must be selected by at least one trigger documented in subsection 6.1.2.
5. **Jet cleaning:** events must pass the LooseBad WP for jet cleaning using jets passing preselection criteria in subsection 6.1.1. This is done to remove events with significant number of calorimeter hits from non-prompt sources (e.g. instrumental effects, cosmic ray background, non-collision particles)
6. **Bad muon veto:** events are removed if they contain at least one muon before overlap removal with insufficient p_T resolution.

7. Kinematic selection: events must have exactly two Tight leptons with the same electric charge, or at least three Tight leptons of any charge. The leading lepton must have $p_T > 28$ GeV, and all leptons must satisfy $p_T > 15$ GeV.

Events are separated into two channels based on the number of leptons: same-sign dilepton (SS2L) for events with exactly two leptons of the same charge, or multilepton (ML) for events with three or more leptons.

Further selections are applied based on the lepton flavors present. In the SS2L channel, if both leptons are electrons, the invariant mass m_{ll} must satisfy $m_{ll} < 81$ GeV and $m_{ll} > 101$ GeV to suppress background involving Z -bosons. In the ML channel, the same criteria must be satisfied for every opposite-sign same-flavor pair of leptons in an event.

6.1.1 Object definition

(electrons, muons, jets)

Jets are reconstructed using particle-flow method with anti- k_t algorithm, using radius parameter $\Delta R = 0.4$.

Each selection comes with associated calibration scale factors to account for discrepancies between data and MC simulation, and are applied multiplicatively to the MC event weights.

Jets containing b -hadrons are identified and tagged with the **GN2v01** algorithm, described in subsection 5.2.1. For this analysis, a jet is considered b -tagged if it passes the 85% WP; this gives the best sensitivity to the signal as shown in Table 6.1.1. A PCBT score is used to quantify the complete output of the b -tagging process for a qualifying jet, with values ranging from 1 to 6 corresponding respectively to the jet not passing any WP, to the jet passing all five WPs.

Selection	Electrons	Muons	Jets
p_T [GeV]	> 15 $p_T(l_0) > 28$	> 15	> 20
$ \eta $	$1.52 \leq \eta < 2.47$ < 1.37	< 2.5	< 2.5
Identification	TightLH pass ECIDS ($ee/e\mu$)	Medium	NNJvt FixedEffPt ($p_T < 60$, $ \eta < 2.4$)
Isolation	Tight_VarRad	PflowTight_VarRad	
Track-vertex assoc.			
$ d_0^{\text{BL}}(\sigma) $	< 5	< 3	
$ \Delta z_0^{\text{BL}} \sin \theta $ [mm]	< 0.5	< 0.5	

Table 6.1: Caption

The E_T^{miss} reconstruction also applies the NNJvt algorithm to jets, and uses the Tight WP for this analysis.

Lepton p_T cut

(lepton p_T cut study: 7 GeV vs 15 GeV)

b -tagging optimization

(WP optimization study)

Trigger	Data period			
	2015	2016	2017	2018
Single electron triggers				
HLT_e24_lhmedium_L1EM20VH	✓	-	-	-
HLT_e60_lhmedium	✓	-	-	-
HLT_e120_lhloose	✓	-	-	-
HLT_e26_lhtight_nod0_ivarloose	-	✓	✓	✓
HLT_e60_lhmedium_nod0	-	✓	✓	✓
HLT_e140_lhloose_nod0	-	✓	✓	✓
Di-electron triggers				
HLT_2e12_lhloose_L12EM10VH	✓	-	-	-
HLT_2e17_lhvloose_nod0	-	✓	-	-
HLT_2e24_lhvloose_nod0	-	-	✓	✓
HLT_2e17_lhvloose_nod0_L12EM15VHI	-	-	-	✓
Single muon trigger				
HLT_mu20_iloose_L1MU15	✓	-	-	-
HLT_mu40	✓	-	-	-
HLT_mu26_ivarmedium	-	✓	✓	✓
HLT_mu50	-	✓	✓	✓

Table 6.2: Caption

6.1.2 Trigger selection

6.1.3 Event categorization

Simulated events are categorized using truth information of leptons (e/μ) and their originating MC particle (mother-particle).

Each lepton can be classified as either prompt or non-prompt, with non-prompt leptons further categorized for background estimation purposes.

If an event contains only prompt leptons, the event is classified as its corresponding process.

If the event contains one non-prompt lepton, the event is classified as the corresponding type of the non-prompt lepton. If the event contains more than one non-prompt lepton, the event

is classified as other.

- **Prompt:** if the lepton originates from $W/Z/H$ boson decays, or from a mother-particle created by a final state photon.
- **Non-prompt:**
 - **Charge-flip (e only):** if the reconstructed charge of the lepton differs from that of the first mother-particle.
 - **Material conversion (e only):** if the lepton originated from a photon conversion and the mother-particle is an isolated prompt photon, non-isolated final state photon, or heavy boson.
 - **γ -conversion (e only):** if the lepton originated from a photon conversion and the mother-particle is a background electron.
 - **Heavy flavor decay:** if the lepton originated from a b - or c -hadron.
 - **Fake:** if the lepton originated from a light- or s -hadron, or if the truth type of the lepton is hadron.
 - **Other:** any lepton that does not belong to one of the above categories.

6.2 Analysis regions

Events are selected and categorized into analysis regions belonging to one of two types: control regions (CRs) enriched in background events, and signal regions (SRs) enriched in signal events. This allows for the examination and control of backgrounds and systematic uncertainties, as well as study of signal sensitivities.

The signal is then extracted from the SRs with a profile LH fit using all regions.

6.2.1 Signal regions

[include blinding strategy]

- All events selected for SS2L and 3L signal regions must satisfy the following criteria:

- Contains 6 or more jets, with at least 2 jets b -tagged at the 85% WP
- Scalar sum of the transverse momenta of all leptons and jets $H_T > 500$ GeV
- Dilepton invariant mass $m_{\ell\ell}$ does not coincide with the Z -boson mass range of $81 - 101$ GeV

- The SR is further granularized by the number of b -jets and leptons to further study and improve signal sensitivity

SR	Selection criteria	
	b -jets	leptons
2b2l	$N_b = 2$	$N_l = 2$
2b3l4l	$N_b = 2$	$N_l \geq 3$
3b2l	$N_b = 3$	$N_l = 2$
3b3l4l	$N_b = 3$	$N_l \geq 3$
4b	$N_b = 4$	

Table 6.3: Caption

(4L study)

6.2.2 Control regions

Control regions are defined for each background to be enriched in the targeted background events, in order to maximize the targeted background's purity and minimize contamination

from other sources within the region.

This helps to constrain and reduce correlation between background normalization factors.

Fit variables and selection criteria are determined via optimization studies on CRs to achieve the largest discriminating power possible between the target background and other event types.

$t\bar{t}W$ background CRs

Two types of CRs are defined to estimate the flavor composition and normalization of $t\bar{t}W$ +jets background: CR $t\bar{t}W^\pm$ +jets to constrain flavor composition, and CR 1b(\pm) to constrain jet multiplicity spectrum.

These are further split into CR $t\bar{t}W^\pm$ and CR 1b(\pm) due to the pronounced asymmetry in $t\bar{t}W$ production from pp collisions, with $t\bar{t}W^+$ being produced at approximately twice the rate of $t\bar{t}W^-$. Selections on H_T and N_{jets} to ensure orthogonality to SR

Selections on total charge for each charged W^\pm boson

Fake/non-prompt background CRs

Selection for fake/non-prompt CRs are determined using the `DFCommonAddAmbiguity` (DFCAA) variable for reconstructed leptons.

DFCAA	Description
-1	No 2nd track found
0	2nd track found, no conversion found
1	Virtual photon conversion candidate
2	Material conversion candidate

Table 6.4: Caption

Four CRs for three main types of fake/non-prompt backgrounds: virtual photon (γ^*) conversion, photon conversion in detector material (Mat. Conv.) and heavy flavor decays (HF).

- Low m_γ^* : events with an e^+e^- pair produced from a virtual photon

Selects two same-sign leptons with at least one electron reconstructed as an internal conversion candidate and neither as with a material conversion candidate ($\text{DFCAA}_{\ell_1(\ell_2)} = 1$ and $\neq 2$)

NF constrained using yield count only.

- Mat. Conv.: events with an electron originating from photon conversion within the detector material.

Selects two same-sign leptons with at least one electron reconstructed as a material conversion candidate ($\text{DFCAA}_{\ell_1(\ell_2)} = 2$).

NF constrained using yield count only.

- HF e/μ : events with a reconstructed non-prompt lepton from semi-leptonic decays of b - and c -hadrons (heavy flavor decays)

Selects three leptons with at least two electrons/muons, with no lepton reconstructed as a conversion candidate ($\text{DFCAA} < 0$).

NFs constrained by fitting with p_T of the third leading lepton ℓ_3 .

6.2.3 Validation regions

In addition, validation regions are also defined to validate the normalization and modeling of $t\bar{t}Z$ and $t\bar{t}W$ background without being used in the fit.

- $t\bar{t}Z$: Selects events with at least two b -tagged jets, at least four total jets and three leptons with at least one same-flavor opposite-sign lepton pair possessing invariant mass $m_{\ell\ell}$ within the Z -boson mass window of $81 - 101$ GeV
- $t\bar{t}W$: Main charge asymmetric background leaning $t\bar{t}W^+$, validated using the difference in number of positively and negatively charged events $N_+ - N_-$ instead of total number of events.

Selects using CR $t\bar{t}W$ and CR 1b criteria, with one VR not orthogonal to SR and one orthogonal VR with more limited statistics.

6.3 Background estimation

Background events in this analysis consist of SM processes that can result in a $t\bar{t}t\bar{t}$ SSML final state.

Can be divided into two types: reducible and irreducible.

Reducible background consists of processes that do not result in SSML final state physically, but are reconstructed as such due to erroneous detector and reconstruction effects.

Three main types: charge misidentification (QmisID), fake leptons and non-prompt leptons. Estimated using template fitting method to adjust MC predictions via floating normalization factors constrained in the CRs.

Irreducible background consists of SM processes that result in SSML final states physically, with all leptons being prompt.

Main irreducible background considered in this analysis: $t\bar{t}t\bar{t}$, $t\bar{t}W$, $t\bar{t}Z$, and $t\bar{t}H$ with smaller contributions from VV , VVV , VH and rarer processes like $t\bar{t}VV$, tWZ , tZq and $t\bar{t}t$.

Region	Channel	N_{jets}	N_b	Other selections	Fitted variable
CR Low m_{γ^*}	SS $e\ell$	[4, 6)	≥ 1	ℓ_1/ℓ_2 is from virtual photon decay $\ell_1 + \ell_2$ not from material conversion	event yield
CR Mat. Conv.	SS $e\ell$	[4, 6)	≥ 1	ℓ_1/ℓ_2 is from material conversion	event yield
CR HF μ	$\ell\mu\mu$	≥ 1	1	$\ell_1 + \ell_2$ not conversion candidates $100 < H_T < 300$ GeV $E_T^{\text{miss}} > 35$ GeV total charge = ± 1	$p_T(\ell_3)$
CR HF e	$e\ell\ell$	≥ 1	1	$\ell_1 + \ell_2$ not conversion candidates $100 < H_T < 275$ GeV $E_T^{\text{miss}} > 35$ GeV total charge = ± 1	$p_T(\ell_3)$
CR $t\bar{t}W^+$	SS $\ell\mu$	≥ 4	≥ 2	$ \eta(e) < 1.5$ for $N_b = 2$: $H_T < 500$ GeV or $N_{\text{jets}} < 6$ for $N_b \geq 3$: $H_T < 500$ GeV total charge > 0	N_{jets}
CR $t\bar{t}W^-$	SS $\ell\mu$	≥ 4	≥ 2	$ \eta(e) < 1.5$ for $N_b = 2$: $H_T < 500$ GeV or $N_{\text{jets}} < 6$ for $N_b \geq 3$: $H_T < 500$ GeV total charge < 0	N_{jets}
CR 1b(+)	SS2L+3L	≥ 4	1	$\ell_1 + \ell_2$ not from material conversion $H_T > 500$ GeV total charge > 0	N_{jets}
CR 1b(-)	SS2L+3L	≥ 4	1	$\ell_1 + \ell_2$ not from material conversion $H_T > 500$ GeV total charge < 0	N_{jets}
VR $t\bar{t}Z$	3L $\ell^\pm\ell^\mp$	≥ 4	≥ 2	$m_{\ell\ell} \in [81, 101]$ GeV	$N_{\text{jets}}, m_{\ell\ell}$
VR $t\bar{t}W + 1b$	SS2L+3L			CR $t\bar{t}W^\pm$ CR 1b(\pm)	N_{jets}
VR $t\bar{t}W + 1b + \text{SR}$	SS2L+3L			CR $t\bar{t}W^\pm$ CR 1b(\pm) SR	N_{jets}
SR	SS2L+3L	≥ 6	≥ 2	$H_T > 500$ GeV $m_{\ell\ell} \notin [81, 101]$ GeV	H_T

Table 6.5: Caption

Most irreducible backgrounds are estimated using MC simulations normalized to their theoretical SM cross sections (template fitting), with the exception of $t\bar{t}W$ background due to MC mismodeling of the process at high jet multiplicities.

The $t\bar{t}W$ is instead given four dedicated CRs, and estimated using a data-driven method with a fitted function parameterized in N_{jets}

All CRs and SR are included in the final LH-fit to data.

6.3.1 Template fitting for fake/non-prompt estimation

Template fit method is a semi-data-driven approach that estimates fake/non-prompt background distributions by fitting the MC kinematic profiles of background processes arising from fake/non-prompt leptons to data.

Each of the four main sources of fake/non-prompt leptons is assigned a free-floating normalization factor constrained by a CR enriched with the corresponding background. The NFs are determined simultaneously with the signal.

- $\text{NF}_{\text{HF } e(\mu)}$: events with one reconstructed non-prompt electron (muon) from heavy flavor decays,
- $\text{NF}_{\text{Mat. Conv.}}$: events with one reconstructed non-prompt electrons from photon conversion in the detector material
- $\text{NF}_{\text{Low } m_{\gamma^*}}$: events with one reconstructed non-prompt electrons in an e^+e^- pair from virtual photon (γ^*) conversion.

6.3.2 Charge misidentification data-driven estimation

The same-sign di-lepton channel in the analysis gives rise to a major background contamination in opposite-sign di-lepton events with one misidentified charge.

Charge misidentification occurs via incorrect track curvature measurements or trident electron contamination from bremsstrahlung, and therefore mainly concerns electrons due to muons' low bremsstrahlung rate and precise curvature information using the ID and MS.

The charge misidentification rates is significant at higher p_T and varies with $|\eta|$ as a proxy for the amount of detector material the electron interacted with, and is consequently estimated in this analysis using a data-driven method with assistance from ECIDS.

The charge flip probability ϵ is estimated using a sample of $Z \rightarrow e^+e^-$ events with additional constraints on the invariant mass m_{ee} to be within 10 GeV of the Z -boson mass.

The Z -boson mass window is defined to be within 4σ to include most events within the peak, and is determined by fitting the m_{ee} spectrum of the two leading electrons to a Breit-Wigner function, resulting in a range of $[65.57, 113.49]$ for SS events and $[71.81, 109.89]$ for OS events. Background contamination near the peak is assumed to be uniform and subtracted using a sideband method.

Since the Z -boson decay products consist of a pair of opposite-sign electrons, all same-sign electron pairs are considered to be affected by charge misidentification.

Assuming the charge flip probabilities of electrons in an event are uncorrelated, the number of events with same-sign electrons N_{ij}^{SS} with the leading electron in the i^{th} 2D bin in $(p_T, |\eta|)$ and the sub-leading electron in the j^{th} bin can be estimated as

$$N_{ij}^{\text{SS}} = N_{ij}^{\text{tot}}(\epsilon_i(1 - \epsilon_j) + \epsilon_j(1 - \epsilon_i)), \quad (6.1)$$

where N_{ij}^{tot} is the total number of events in the i^{th} and j^{th} bin regardless of charge, and $\epsilon_{i(j)}$ is the charge flip rate in the $i^{\text{th}}(j^{\text{th}})$ bin.

Assuming N_{ij}^{SS} follows a Poisson distribution around the expectation value \bar{N}_{ij}^{SS} , the charge flip rate ϵ can be estimated by minimizing a negative-LLH function parameterized in p_{T} and $|\eta|$,

$$\begin{aligned}
-\ln(\mathcal{L}(\epsilon|N_{\text{SS}})) &= -\ln \prod_{ij} \frac{(N_{ij}^{\text{tot}})^{N_{ij}^{\text{SS}}} \cdot e^{-N_{ij}^{\text{tot}}}}{N_{ij}^{\text{SS}}!} \\
&= -\sum_{ij} \left[N_{ij}^{\text{SS}} \ln(N_{ij}^{\text{tot}}(\epsilon_i(1-\epsilon_j) + \epsilon_j(1-\epsilon_i))) - N_{ij}^{\text{tot}}(\epsilon_i(1-\epsilon_j) + \epsilon_j(1-\epsilon_i)) \right].
\end{aligned} \tag{6.2}$$

$$\tag{6.3}$$

The charge flip rate is then calculated separately for SR and CRs with different electron definitions (CR Low m_{γ^*} , CR Mat. Conv., CR $t\bar{t}W$) using events satisfying 2LSS kinematic selections but with OS electrons, after applying region-specific lepton selections and ECIDS. The following weight is applied to OS events to correct for misidentified SS events within the region:

$$w = \frac{\epsilon_i + \epsilon_j - 2\epsilon_i\epsilon_j}{1 - \epsilon_i - \epsilon_j + 2\epsilon_i\epsilon_j}. \tag{6.4}$$

6.3.3 $t\bar{t}W$ background data-driven estimation

- $t\bar{t}W$ represents a major source of irreducible background contamination in SM and BSM analyses with $t\bar{t}t\bar{t}$ final states.
- Measured cross section for $t\bar{t}W$ background has been consistently higher than predicted values as seen in previous analyses ($t\bar{t}H/t\bar{t}W$ multilepton [1][11], $t\bar{t}t\bar{t}$ analyses [8][17]) due to mismodeling, especially at higher N_{jets}

(show postfit $t\bar{t}W$ VR distribution)

- Previously, this was handled by assigning large ad-hoc systematic uncertainties to $t\bar{t}W$ events with 7 or more jets.
- A semi-data-driven method originally employed in the R-parity-violating-supersymmetry search [20] was used to mitigate this problem.
- This method was shown to be effective in the SM $t\bar{t}t\bar{t}$ observation analysis [17] by improving $t\bar{t}W$ modeling especially in the showering step and switching $t\bar{t}W$ systematic uncertainties from predominantly modeling to statistical.
- MC kinematic distributions for $t\bar{t}W$ are applied with correction factors obtained from a fitted function parameterized in N_{jets} .
- The function describes scaling patterns for QCD [26] can be represented by ratio of successive exclusive jet cross-sections

$$R_{(n+1)/n} = e^{-b} + \frac{\bar{n}}{n+1} = a_0 + \frac{a_1}{1+(j-4)}, \quad (6.5)$$

where n is the number of jets in addition to the hard process, j is the inclusive number of jets, and \bar{n} is the expectation value for the Poisson distribution for exclusive jet cross-section at jet multiplicity n , described as $P_n = \sigma_n/\sigma_{\text{tot}}$.

- Same-sign di-lepton $t\bar{t}W$ events dominate the $t\bar{t}W$ background and produce 4 jets in the matrix element at tree level for the hard process, so n is defined starting from 5 jets and j is defined as inclusive number of jets with 4 or more jets, or $j \equiv n + 4$.
- The two terms in the equation correspond respectively to staircase and Poisson scaling between successive multiplicity cross sections, defined as constant ratios e^{-b} and ratios between Poisson probability for $n+1$ and n jets. Staircase scaling is sensitive to events with high jet multiplicity, while Poisson scaling is sensitive to events with low jet multiplicity [26].

- The scaling pattern can then be re-parameterized in a_0 and a_1 to obtain the $t\bar{t}W$ yield at j'

$$\text{Yield}_{t\bar{t}W(j')} = \text{Yield}_{t\bar{t}W(j=4)} \times \prod_{j=4}^{j'-1} \left(a_0 + \frac{a_1}{1 + (j - 4)} \right) \quad (6.6)$$

where j' is defined as $j' \equiv j + 1$ with $j \geq 4$ since the parameterization starts at the 4th jet.

The $t\bar{t}W$ yield at the 4-jet bin can be represented by a normalization factor applied to $t\bar{t}W$ MC simulation as $\text{Yield}_{t\bar{t}W(j=4)} = \text{NF}_{t\bar{t}W(j=4)} \times \text{MC}_{j=4}$.

To account for the disparity in $t\bar{t}W^+$ and $t\bar{t}W^-$ cross-section, assuming the scaling is the same for both processes, $\text{NF}_{t\bar{t}W(j=4)}$ can be further split into $\text{NF}_{t\bar{t}W^+(j=4)}$ and $\text{NF}_{t\bar{t}W^-(j=4)}$. Both NFs are left free-floating to constrain $t\bar{t}W$ yields at the 4-jet bin in CR 1b(+) and CR 1b(-).

The final N_{jets} -parameterized function can then be represented by $\text{NF}_{t\bar{t}W(j')}$ as

$$\text{NF}_{t\bar{t}W(j')} = \left(\text{NF}_{t\bar{t}W^+(j=4)} + \text{NF}_{t\bar{t}W^-(j=4)} \right) \times \prod_{j=4}^{j'-1} \left(a_0 + \frac{a_1}{1 + (j - 4)} \right). \quad (6.7)$$

This normalization is calculated and applied separately for each sub-sample of $t\bar{t}W^+$ and $t\bar{t}W^-$ in an N_{jets} bin for $4 \leq N_{\text{jets}} < 10$.

Due to small contributions in the CRs, events with $N_{\text{jets}} < 4$ and $N_{\text{jets}} \geq 10$ are not normalized with this scheme.

Instead, $N_{\text{jets}} < 4$ $t\bar{t}W$ events are fitted by propagating normalization in the 4-jet bin without additional shape correction. The correction factor for $t\bar{t}W$ events with $N_{\text{jets}} \geq 10$ is obtained by summing up the overflow from $N_{\text{jets}} = 10$ to $N_{\text{jets}} = 12$, described as $\sum_{j'=10}^{12} \prod_{j=4}^{j'-1} \left(a_0 + \frac{a_1}{1 + (j - 4)} \right)$. Events with $N_{\text{jets}} \geq 13$ are negligible and thus not included in the sum.

Control region definitions

Four control regions CR $t\bar{t}W^+$, CR $t\bar{t}W^-$, CR 1b(+), CR 1b(-) are constructed to fit $\text{NF}_{t\bar{t}W^\pm(j=4)}$ and the scaling parameters a_0, a_1 for the $t\bar{t}W$ background, as well as validating the parameterization.

Events in CR $t\bar{t}W^\pm$ are required to contain at least two b -tagged jets similar to the SR to determine the $t\bar{t}W$ normalization within an SR-related phase space. Orthogonality with SR is satisfied by requiring $H_T < 500$ GeV or $N_{\text{jets}} < 6$ when $N_b = 2$, and $H_T < 500$ GeV when $N_b \geq 3$.

The remaining CR 1b(\pm) require events to have $H_T > 500$ GeV and at least four jets to encompass events with high N_{jets} , which can be used to determine the $t\bar{t}W$ jet multiplicity spectrum for fitting $a_{0,1}$. The selection criteria also include exactly one b -tagged jet to maintain orthogonality with SR. Assuming the $t\bar{t}W$ jet multiplicity distribution is similar across different N_b , a fitted N_{jets} distribution in CR 1b(\pm) can be used to describe the $t\bar{t}W$ parameterization at higher N_{jets} . The full selection criteria for all four regions are shown in Table 6.5

Validating the $t\bar{t}W$ parameterization in Equation 6.7 makes use of the unique charge asymmetry in $t\bar{t}W$ production that's not present in other background or signal processes. The number of events with all negatively charged leptons is subtracted from that of events with all positively charged leptons, which cancels out charge symmetric events and leaves the $t\bar{t}W$ background. Validation is done via a statistical-only (stat-only) fit to the $t\bar{t}W$ MC prediction in CR 1b(\pm). [validation results](#)

6.3.4 $t\bar{t}Z$ background validation

Chapter 7. Systematic Uncertainties

(nuisance parameters)

7.1 Experimental uncertainties

Instrumental & minor:

- uncertainty on the integrated luminosity of the 2015-2018 Run 2 data set is 0.83%, obtained by the LUCID-2 detector for the primary luminosity measurements complemented by the ID and calorimeters
- Pile-up modeling in MC was calibrated to data through pile-up reweighting, resulting in a set of calibration SFs and associated uncertainties.

In general, calibrating MC simulations to match performance in data incurs uncertainties associated with the MC-to-data scale factors obtained from the calibration, which are in turn propagated to observables in the analysis.

7.1.1 Leptons

The trigger/reconstruction/ID/isolation efficiencies of electrons and muons (with separate systematic and statistical components for muon) differ between MC simulation and data, and require correction in the form of SFs with its associated uncertainties.

Similarly, electron and muon energy-momentum scale and resolution also incur uncertainties from MC-to-data correction, calculated by varying scale and resolution during simulations. Muons have additional uncertainties for charge-dependent and charge-independent momentum scale, and detector-specific (ID, MS, CB) track resolution.

The charge identification/ECIDS efficiency also gives rise to an additional uncertainty component.

7.1.2 Jets

Experimental uncertainties on jets are dominated by flavor tagging-related uncertainties, with subleading contributions from jet energy scale/resolution (JES/JER) and NNJvt calibration.

Jet energy scale

JES and its associated uncertainties are determined using data from test-beam and LHC collisions and MC simulated samples, decomposed into uncorrelated components:

- Effective nuisance parameters (NPs): 15 p_T -dependent uncertainty components in total measured in situ, grouped based on their origin (2 detector-related, 4 modeling-related, 3 mixed, 6 statistical-related)
- η intercalibration: 6 total components (1 modeling-related, 4 non-closure and 1 statistical-related) associated with the correction of the forward jets' ($0.8 \leq |\eta| < 4.5$) energy scale to that of the central jets ($|\eta| < 0.8$).
- Flavor composition/response: 2 components for relative quark-gluon flavor compositions in background and signal samples, and 2 components for uncertainty in responses to gluon-initiated versus quark-initiated jets

- Pile-up subtraction: 4 components, two for uncertainty in μ (**OffsetMu**) and N_{PV} (**OffsetNPV**) modeling, one for residual p_{T} -dependency (**PtTerm**) and one for topology dependence on the per-event p_{T} density modeling (**RhoTopology**)
- Punch-through effect treatment: two terms (AF3 fast simulation and full detector simulations) for GSC punch-through jet response correction between data and MC.
- Non-closure: one term to account for difference between AF3-simulated samples and full detector simulations.
- High- p_{T} single-particle response: one term for response to high- p_{T} jets from single-particle and test-beam measurements
- b -jets response: one term for uncertainty in the response to b -jets

Jet energy resolution

JER measured separately in data and MC simulations using in situ techniques as a function of p_{T} and η for a given jet. Associated uncertainties are defined as quadratic difference between data and MC simulations.

This analysis uses the full JER uncertainty set provided for Run 2 searches with 14 total components: 12 effective NPs and 2 for difference between data and MC simulation, separately for AF3 and FS.

Jet vertex tagging

JVT associated uncertainty is obtained by varying the JVT efficiency correction SFs within their range of uncertainty. This uncertainty accounts for remaining contamination from pile-up jets after applying pile-up suppression and MC generator choice.

Flavor tagging

SFs for b -jets tagging efficiencies and c -/light-jets mis-tagging rates are obtained as a function of p_T for b -/ c -/light-jets and PCB scores. The covariance matrix of systematic and statistical uncertainties is diagonalized and reduced in dimensions using principle component analysis (PCA), resulting in a set of orthogonal NPs: 85 for b -jets, 56 for c -jets and 42 for light-jets.

7.1.3 Missing transverse energy

Uncertainties for E_T^{miss} arise from possible miscalibration of its soft-track component, and are estimated using data-MC comparison of the p_T scale and resolution between the hard and soft E_T^{miss} terms. These uncertainties are represented by three independent terms: one for scale uncertainty and two resolution uncertainties for the parallel and perpendicular components.

7.2 Modeling uncertainties

7.2.1 Signal and irreducible background uncertainties

7.2.2 Reducible background uncertainties

Systematic uncertainty	Terms	Scale [%]
Event		
Luminosity	1	0.83
Pile-up reweighting	1	$\mathcal{O}(1) \sim \mathcal{O}(10)$
Electrons		
Trigger efficiency	1	$\mathcal{O}(10^{-2}) \sim \mathcal{O}(10^{-1})$
Reconstruction efficiency [†]	1	$\mathcal{O}(10^{-1}) \sim \mathcal{O}(1)$
Identification efficiency [†]	1	$\mathcal{O}(10^{-1}) \sim \mathcal{O}(1)$
Isolation efficiency [†]	1	$\mathcal{O}(10^{-1}) \sim \mathcal{O}(1)$
Energy scale	1	$\mathcal{O}(10^{-2}) \sim \mathcal{O}(10^{-1})$
Energy resolution	1	$\mathcal{O}(10^{-2}) \sim \mathcal{O}(10^{-1})$
Charge identification (ECIDS) efficiency [†]	1	$\mathcal{O}(10^{-1}) \sim \mathcal{O}(1)$
Muons		
Trigger efficiency (stat/sys)	2	$\mathcal{O}(10^{-1}) \sim \mathcal{O}(1)$
Track-to-vertex association efficiency (stat/sys)	2	$\mathcal{O}(10^{-2}) \sim \mathcal{O}(10^{-1})$
Reconstruction/identification efficiency (stat/sys)	2	$\mathcal{O}(10^{-1}) \sim \mathcal{O}(1)$
Low- p_T (< 15 GeV) reconstruction/identification efficiency (stat/sys)	2	$\mathcal{O}(10^{-1}) \sim \mathcal{O}(1)$
Isolation efficiency (stat/sys)	2	$\mathcal{O}(10^{-1}) \sim \mathcal{O}(1)$
Charge-independent momentum scale	1	$\mathcal{O}(10^{-2}) \sim \mathcal{O}(10^{-1})$
Charge-dependent momentum scale	4	$\mathcal{O}(10^{-2}) \sim \mathcal{O}(10^{-1})$
Energy resolution (CB)	1	$\mathcal{O}(10^{-2}) \sim \mathcal{O}(10^{-1})$
Energy resolution (ID & MS)*	2	$\mathcal{O}(10^{-2}) \sim \mathcal{O}(10^{-1})$
Jets		
JES effective NP	15	$\mathcal{O}(10^{-2}) \sim \mathcal{O}(1)$
JES η intercalibration	3	$\mathcal{O}(10^{-1}) \sim \mathcal{O}(1)$
JES flavor composition	2	$\mathcal{O}(10^{-1}) \sim \mathcal{O}(1)$
JES flavor response	1	$\mathcal{O}(10^{-1}) \sim \mathcal{O}(1)$
JES pile-up	4	$\mathcal{O}(10^{-1}) \sim \mathcal{O}(10)$
JES punch-through (FS/AF3*)	2	$< \mathcal{O}(10^{-2})$
JES non-closure	1	$\mathcal{O}(10^{-2}) \sim \mathcal{O}(10^{-1})$
JES high- p_T single particle	1	$< \mathcal{O}(10^{-2})$
JES b -jet response	1	$\mathcal{O}(10^{-1}) \sim \mathcal{O}(1)$
JER effective NP	12	$\mathcal{O}(10^{-1}) \sim \mathcal{O}(1)$
JER data/MC (FS/AF3*)	2	$\mathcal{O}(10^{-1}) \sim \mathcal{O}(1)$
JVT efficiency	1	$\mathcal{O}(10^{-1}) \sim \mathcal{O}(1)$
GN2v01 b -tagging efficiency (b -jets)	85	$\mathcal{O}(10^{-2}) \sim \mathcal{O}(1)$
GN2v01 b -tagging efficiency (c -jets)	56	$\mathcal{O}(10^{-2}) \sim \mathcal{O}(1)$
GN2v01 b -tagging efficiency (light-jets)	42	$\mathcal{O}(10^{-2}) \sim \mathcal{O}(1)$
E_T^{miss}-Terms		
Track-based soft term for transversal resolution	1	$\mathcal{O}(10^{-2}) \sim \mathcal{O}(10^{-1})$
Track-based soft term for longitudinal resolution	1	$\mathcal{O}(10^{-2}) \sim \mathcal{O}(10^{-1})$
Track-based soft term for longitudinal scale	1	$\mathcal{O}(10^{-2}) \sim \mathcal{O}(10^{-1})$

Table 7.1: Summary of the experimental systematic uncertainties considered in this analysis.

Systematic uncertainty	Terms	Scale [%]
$t\bar{t}Z'$ modeling		
Renormalization & factorization scale PDF		
SM $t\bar{t}t\bar{t}$ modeling		
Cross-section Renormalization & factorization scale PDF Generator choice Parton shower model		
SM $t\bar{t}t$ modeling		
Cross-section Renormalization & factorization scale PDF Additional b -jets		
$t\bar{t}W$ modeling		
Renormalization & factorization scale Generator choice Additional b -jets		
$t\bar{t}Z$ modeling		
Cross-section Renormalization & factorization scale PDF Generator choice Additional b -jets		
$t\bar{t}H$ modeling		
Cross-section Renormalization & factorization scale PDF Generator choice Parton shower model Additional b -jets		
Other background modeling		
Cross-section Additional b -jets		

Table 7.2: Summary of the experimental systematic uncertainties considered in this analysis.

Chapter 8. Results

8.1 Profile likelihood fit

- Plain Asimov fit
- Real CRs-only fit
- Real SR-blinded fit
- Real SR-unblinded fit

8.2 Fit results

8.3 Limits

8.4 Interpretation

Chapter 9. Summary

References

- [1] ATLAS Collaboration. *Analysis of $t\bar{t}H$ and $t\bar{t}W$ production in multilepton final states with the ATLAS detector*. ATLAS-CONF-2019-045. 2019. URL: <https://cds.cern.ch/record/2693930> (cit. on p. 49).
- [2] ATLAS Collaboration. *ATLAS b -jet identification performance and efficiency measurement with $t\bar{t}$ events in pp collisions at $\sqrt{s} = 13$ TeV*. In: *The European Physical Journal C* 79.11 (2019), p. 970. ISSN: 1434-6052. DOI: [10.1140/epjc/s10052-019-7450-8](https://doi.org/10.1140/epjc/s10052-019-7450-8). arXiv: [1907.05120](https://arxiv.org/abs/1907.05120) [[hep-ex](#)] (cit. on p. 25).
- [3] ATLAS Collaboration. *Dependence of the Jet Energy Scale on the Particle Content of Hadronic Jets in the ATLAS Detector Simulation*. ATL-PHYS-PUB-2022-021. 2022. URL: <https://cds.cern.ch/record/2808016> (cit. on p. 26).
- [4] ATLAS Collaboration. *Electron and photon performance measurements with the ATLAS detector using the 2015–2017 LHC proton–proton collision data*. In: *JINST* 14 (2019), P12006. DOI: [10.1088/1748-0221/14/12/P12006](https://doi.org/10.1088/1748-0221/14/12/P12006). arXiv: [1908.00005](https://arxiv.org/abs/1908.00005) [[hep-ex](#)] (cit. on pp. viii, 27, 29, 31, 32).
- [5] ATLAS Collaboration. *Electron Identification with a Convolutional Neural Network in the ATLAS Experiment*. ATL-PHYS-PUB-2023-001. 2023. URL: <https://cds.cern.ch/record/2850666> (cit. on p. 31).

- [6] ATLAS Collaboration. *Electron reconstruction and identification in the ATLAS experiment using the 2015 and 2016 LHC proton–proton collision data at $\sqrt{s} = 13$ TeV*. In: *Eur. Phys. J. C* 79 (2019), p. 639. DOI: [10.1140/epjc/s10052-019-7140-6](https://doi.org/10.1140/epjc/s10052-019-7140-6). arXiv: [1902.04655](https://arxiv.org/abs/1902.04655) [[physics.ins-det](#)] (cit. on pp. viii, 27–29, 31).
- [7] ATLAS Collaboration. *E_T^{miss} performance in the ATLAS detector using 2015–2016 LHC pp collisions*. ATLAS-CONF-2018-023. 2018. URL: <https://cds.cern.ch/record/2625233> (cit. on p. 36).
- [8] ATLAS Collaboration. *Evidence for $t\bar{t}t\bar{t}$ production in the multilepton final state in proton–proton collisions at $\sqrt{s} = 13$ TeV with the ATLAS detector*. In: *Eur. Phys. J. C* 80 (2020), p. 1085. DOI: [10.1140/epjc/s10052-020-08509-3](https://doi.org/10.1140/epjc/s10052-020-08509-3). arXiv: [2007.14858](https://arxiv.org/abs/2007.14858) [[hep-ex](#)] (cit. on p. 49).
- [9] ATLAS Collaboration. *Graph Neural Network Jet Flavour Tagging with the ATLAS Detector*. ATL-PHYS-PUB-2022-027. 2022. URL: <https://cds.cern.ch/record/2811135> (cit. on pp. viii, 26).
- [10] ATLAS Collaboration. *Improved electron reconstruction in ATLAS using the Gaussian Sum Filter-based model for bremsstrahlung*. ATLAS-CONF-2012-047. 2012. URL: <https://cds.cern.ch/record/1449796> (cit. on p. 22).
- [11] ATLAS Collaboration. *Measurement of the total and differential cross-sections of $t\bar{t}W$ production in pp collisions at $\sqrt{s} = 13$ TeV with the ATLAS detector*. In: *JHEP* 05 (2024), p. 131. DOI: [10.1007/JHEP05\(2024\)131](https://doi.org/10.1007/JHEP05(2024)131). arXiv: [2401.05299](https://arxiv.org/abs/2401.05299) [[hep-ex](#)] (cit. on p. 49).

- [12] ATLAS Collaboration. *Measurements of b -jet tagging efficiency with the ATLAS detector using $t\bar{t}$ events at $\sqrt{s} = 13$ TeV*. In: *JHEP* 08 (2018), p. 089. DOI: [10.1007/JHEP08\(2018\)089](https://doi.org/10.1007/JHEP08(2018)089). arXiv: [1805.01845](https://arxiv.org/abs/1805.01845) [[hep-ex](#)] (cit. on p. 25).
- [13] ATLAS Collaboration. *Measuring the b -jet identification efficiency for high p_T jets using multijet events in proton–proton collisions at $\sqrt{s} = 13$ TeV recorded with the ATLAS detector*. ATL-PHYS-PUB-2022-010. 2022. URL: <https://cds.cern.ch/record/2804062> (cit. on p. 26).
- [14] ATLAS Collaboration. *Muon reconstruction and identification efficiency in ATLAS using the full Run 2 pp collision data set at $\sqrt{s} = 13$ TeV*. In: *Eur. Phys. J. C* 81 (2021), p. 578. DOI: [10.1140/epjc/s10052-021-09233-2](https://doi.org/10.1140/epjc/s10052-021-09233-2). arXiv: [2012.00578](https://arxiv.org/abs/2012.00578) [[hep-ex](#)] (cit. on pp. viii, 33, 34).
- [15] ATLAS Collaboration. *Muon reconstruction performance of the ATLAS detector in proton–proton collision data at $\sqrt{s} = 13$ TeV*. In: *Eur. Phys. J. C* 76 (2016), p. 292. DOI: [10.1140/epjc/s10052-016-4120-y](https://doi.org/10.1140/epjc/s10052-016-4120-y). arXiv: [1603.05598](https://arxiv.org/abs/1603.05598) [[hep-ex](#)] (cit. on p. 33).
- [16] ATLAS Collaboration. *Observation of electroweak production of two jets in association with an isolated photon and missing transverse momentum, and search for a Higgs boson decaying into invisible particles at 13 TeV with the ATLAS detector*. In: *Eur. Phys. J. C* 82 (2022), p. 105. DOI: [10.1140/epjc/s10052-021-09878-z](https://doi.org/10.1140/epjc/s10052-021-09878-z). arXiv: [2109.00925](https://arxiv.org/abs/2109.00925) [[hep-ex](#)] (cit. on pp. vii, 36).
- [17] ATLAS Collaboration. *Observation of four-top-quark production in the multilepton final state with the ATLAS detector*. In: *Eur. Phys. J. C* 83 (2023), p. 496. DOI: [10.1140/epjc/s10052-023-11573-0](https://doi.org/10.1140/epjc/s10052-023-11573-0). arXiv: [2303.15061](https://arxiv.org/abs/2303.15061) [[hep-ex](#)] (cit. on pp. 49, 50).

- [18] ATLAS Collaboration. *Performance of missing transverse momentum reconstruction with the ATLAS detector using proton–proton collisions at $\sqrt{s} = 13$ TeV*. In: *Eur. Phys. J. C* 78 (2018), p. 903. DOI: [10.1140/epjc/s10052-018-6288-9](https://doi.org/10.1140/epjc/s10052-018-6288-9). arXiv: [1802.08168](https://arxiv.org/abs/1802.08168) [[hep-ex](#)] (cit. on p. 35).
- [19] ATLAS Collaboration. *Performance of the ATLAS track reconstruction algorithms in dense environments in LHC Run 2*. In: *Eur. Phys. J. C* 77 (2017), p. 673. DOI: [10.1140/epjc/s10052-017-5225-7](https://doi.org/10.1140/epjc/s10052-017-5225-7). arXiv: [1704.07983](https://arxiv.org/abs/1704.07983) [[hep-ex](#)] (cit. on p. 21).
- [20] ATLAS Collaboration. *Search for R -parity-violating supersymmetry in a final state containing leptons and many jets with the ATLAS experiment using $\sqrt{s} = 13$ TeV proton–proton collision data*. In: *Eur. Phys. J. C* 81 (2021), p. 1023. DOI: [10.1140/epjc/s10052-021-09761-x](https://doi.org/10.1140/epjc/s10052-021-09761-x). arXiv: [2106.09609](https://arxiv.org/abs/2106.09609) [[hep-ex](#)] (cit. on p. 50).
- [21] ATLAS Collaboration. *Topological cell clustering in the ATLAS calorimeters and its performance in LHC Run 1*. In: *Eur. Phys. J. C* 77 (2017), p. 490. DOI: [10.1140/epjc/s10052-017-5004-5](https://doi.org/10.1140/epjc/s10052-017-5004-5). arXiv: [1603.02934](https://arxiv.org/abs/1603.02934) [[hep-ex](#)] (cit. on p. 20).
- [22] T Cornelissen et al. *Concepts, Design and Implementation of the ATLAS New Tracking (NEWT)*. Tech. rep. Geneva: CERN, 2007. URL: <https://cds.cern.ch/record/1020106> (cit. on p. 22).
- [23] T G Cornelissen et al. *The global 2 track fitter in ATLAS*. In: *Journal of Physics: Conference Series* 119.3 (2008), p. 032013. DOI: [10.1088/1742-6596/119/3/032013](https://doi.org/10.1088/1742-6596/119/3/032013). URL: <https://dx.doi.org/10.1088/1742-6596/119/3/032013> (cit. on p. 22).
- [24] Arnaud Duperrin. *Flavour tagging with graph neural networks with the ATLAS detector*. Tech. rep. Presented at DIS2023, Michigan State University, USA. Geneva: CERN,

2023. arXiv: [2306.04415 \[hep-ex\]](#). URL: <https://cds.cern.ch/record/2860610> (cit. on pp. viii, 26).
- [25] R. Frhwirth. *Application of Kalman filtering to track and vertex fitting*. In: *Nuclear Instruments and Methods in Physics Research Section A: Accelerators, Spectrometers, Detectors and Associated Equipment* 262.2 (1987), pp. 444–450. ISSN: 0168-9002. DOI: [https://doi.org/10.1016/0168-9002\(87\)90887-4](https://doi.org/10.1016/0168-9002(87)90887-4). URL: <https://www.sciencedirect.com/science/article/pii/0168900287908874> (cit. on p. 22).
- [26] Erik Gerwick et al. *Scaling Patterns for QCD Jets*. In: *JHEP* 10 (2012), p. 162. DOI: [10.1007/JHEP10\(2012\)162](https://doi.org/10.1007/JHEP10(2012)162). arXiv: [1208.3676 \[hep-ph\]](#) (cit. on p. 50).
- [27] Walter Lampl et al. *Calorimeter Clustering Algorithms: Description and Performance*. ATL-LARG-PUB-2008-002. 2008. URL: <https://cds.cern.ch/record/1099735> (cit. on p. 20).
- [28] Andreas Salzburger and on behalf of the ATLAS Collaboration. *Optimisation of the ATLAS Track Reconstruction Software for Run-2*. In: *Journal of Physics: Conference Series* 664.7 (2015), p. 072042. DOI: [10.1088/1742-6596/664/7/072042](https://doi.org/10.1088/1742-6596/664/7/072042). URL: <https://dx.doi.org/10.1088/1742-6596/664/7/072042> (cit. on p. 22).
- [29] Samuel Van Stroud et al. *FTAG Run-3 Algorithms Performance*. Tech. rep. Geneva: CERN, 2023. URL: <https://cds.cern.ch/record/2872884> (cit. on pp. viii, 26).
- [30] Valentina Vecchio. *Measurement of the b -tagging efficiency using multi-jet events in ATLAS*. Tech. rep. Presented at The Tenth Annual Large Hadron Collider Physics (LHCP2022). Geneva: CERN, 2022. URL: <https://cds.cern.ch/record/2825428> (cit. on p. 26).

- [31] D Wicke. *A New Algorithm for Solving Tracking Ambiguities*. In: (1998). URL: <https://cds.cern.ch/record/2625731> (cit. on p. 22).